The Astrophysical Journal, 991:198 (27pp), 2025 October 1 https://doi.org/10.3847/1538-4357/adfbe0

Quantification of the Age Dependence of Mid-infrared Star Formation Rate Indicators

Daniela Calzetti[1], Robert C. Kennicutt[2,3], Angela Adamo[4], Karin Sandstrom[5], Daniel A. Dale[6], Bruce Elmegreen[7], John S. Gallagher[8,9], Benjamin Gregg[1], Varun Bajaj[10], Torsten Böker[11], Giacomo Bortolini[4], Martha Boyer[10], Matteo Correnti[12,13], Ilse De Looze[14], Bruce T. Draine[15], Ana Duarte-Cabral[16], Helena Faustino Vieira[4], Kathryn Grasha[17,18,34], L. K. Hunt[19], Kelsey E. Johnson[20], Ralf S. Klessen[21,22,23,24], Mark R. Krumholz[25], Thomas S.-Y. Lai[26], Drew Lapeer[1], Sean T. Linden[27], Matteo Messa[28], Göran Östlin[4], Alex Pedrini[4], Mònica Relaño[29,30], Elena Sabbi[31], Eva Schinnerer[32], Evan Skillman[33], Linda J. Smith[10], Monica Tosi[28], Fabian Walter[32], and Tony D. Weinbeck[6]

[1] Department of Astronomy, University of Massachusetts Amherst, 710 North Pleasant Street, Amherst, MA 01003, USA
[2] Department of Physics and Astronomy, Texas A&M University, 578 University Drive, College Station, TX 77843-4242, USA
[3] Steward Observatory, University of Arizona, 933 North Cherry Avenue, Tucson, AZ 85721, USA
[4] Department of Astronomy, The Oskar Klein Centre, Stockholm University, AlbaNova, SE-10691 Stockholm, Sweden
[5] Department of Astronomy & Astrophysics, University of California, San Diego, 9500 Gilman Drive, La Jolla, CA 92093, USA
[6] Department of Physics and Astronomy, University of Wyoming, Laramie, WY 82071, USA
[7] Katonah, NY 10536, USA
[8] Department of Astronomy, University of Wisconsin–Madison, 475 North Charles Street, Madison, WI 53706–1507, USA
[9] Department of Physics and Astronomy, Macalester University, 1600 Grand Avenue, Saint Paul, MN 55105-1899, USA
[10] Space Telescope Science Institute, 3700 San Martin Drive, Baltimore, MD 21218, USA
[11] European Space Agency, c/o STScI, 3700 San Martin Drive, Baltimore, MD 21218, USA
[12] INAF Osservatorio Astronomico di Roma, Via Frascati 33, 00078 Monteporzio Catone, Rome, Italy
[13] ASI-Space Science Data Center, Via del Politecnico, I-00133 Rome, Italy
[14] Department of Physics and Astronomy, University of Ghent, Proeftuinstraat 86, 9000 Gent, Belgium
[15] Department of Astrophysical Sciences, Princeton University, 4 Ivy Lane, Princeton, NJ 08544, USA
[16] Cardiff Hub for Astrophysics Research and Technology (CHART), School of Physics & Astronomy, Cardiff University, The Parade, Cardiff CF24 3AA, UK
[17] Research School of Astronomy and Astrophysics, Australian National University, Canberra, ACT 2611, Australia
[18] ARC Centre of Excellence for All Sky Astrophysics in 3 Dimensions (ASTRO 3D), Australia
[19] INAF—Osservatorio Astrofisico di Arcetri, Largo Enrico Fermi 5, 50125 Firenze, Italy
[20] Department of Astronomy, University of Virginia, Charlottesville, VA, USA
[21] Universität Heidelberg, Zentrum für Astronomie, Institut für Theoretische Astrophysik, Albert-Ueberle-Straße 2, 69120 Heidelberg, Germany
[22] Universität Heidelberg, Interdisziplinäres Zentrum für Wissenschaftliches Rechnen, Im Neuenheimer Feld 225, 69120 Heidelberg, Germany
[23] Harvard | Smithsonian, Center for Astrophysics, 60 Garden Street, Cambridge, MA 02138, USA
[24] Elizabeth S. and Richard M. Cashin Fellow, Radcliffe Institute for Advanced Studies, Harvard University, 10 Garden Street, Cambridge, MA 02138, USA
[25] Research School of Astronomy and Astrophysics, Australian National University, 233 Mount Stromlo Road, Stromlo ACT 2611, Australia
[26] Infrared Processing and Analysis Center, California Institute of Technology, 1200 East California Boulevard, Pasadena, CA 91125, USA
[27] Department of Astronomy and Steward Observatory, University of Arizona, Tucson, AZ 85721, USA
[28] INAF—Osservatorio di Astrofisica e Scienza dello Spazio di Bologna, Via Gobetti 93/3, I-40129 Bologna, Italy
[29] Departmento Física Teòrica y del Cosmos, Universidad de Granada, Campus de Fuentenueva, E-18071 Granada, Spain
[30] Instituto Universitario Carlos I de Física Teórica y Computacional, Universidad de Granada, 18071, Granada, Spain
[31] Gemini Observatory, NOIRLab, 950 North Cherry Avenue, Tucson, AZ 85719, USA
[32] Max Planck Institut für Astronomie, Königstuhl 17, D-69117 Heidelberg, Germany
[33] School of Physics and Astronomy, University of Minnesota, 116 Church Street, Minneapolis, MN 55455, USA
Received 2025 May 13; revised 2025 August 5; accepted 2025 August 8; published 2025 September 29

Abstract

We combine James Webb Space Telescope images of the nearby galaxy NGC 5194 in the hydrogen recombination line Paα (1.8756 μm) from the Cycle 1 program JWST-FEAST with 21 μm dust continuum images from the Cycle 2 Treasury program JWGT to quantify the difference in the calibration of mid-infrared star formation rates (SFRs) between H II regions and galaxies. We use archival Hubble Space Telescope Hα imaging to correct the Paα emission for the effects of dust attenuation. Our data confirm previous results that the dust-corrected Paα flux is tightly correlated with the 21 μm emission at the scales of H II regions. When combined with published JWST data for the H II regions of the galaxy NGC 628 and Spitzer Space Telescope 24 μm data for whole galaxies and for kiloparsec-size galaxy regions, we show that the $L(24)$–$L(\mathrm{Pa}\alpha)$ relation has exponent > 1 across six decades in luminosity. In addition, the hybrid 24 μm + Hα SFR indicator has a scaling constant about 4.4 times higher for H II regions than for whole galaxies, also in agreement with previous results. Models of stellar populations with a range of star formation histories reveal that the observed trends can be entirely ascribed to and quantified with the contribution to the infrared emission by stellar populations older than ~5–6 Myr. Based on the models' results, we provide (1) a calibration for the infrared SFR across 6 orders of magnitude in $L(24)$, from H II

[34] ARC DECRA Fellow.

regions to luminous galaxies, and (2) a prescription for the scaling constant of the hybrid infrared SFR indicators as a function of the star formation timescale.

Unified Astronomy Thesaurus concepts: H II regions (694); Star formation (1569); Star forming regions (1565); Scaling relations (2031); Galaxy stellar content (621)

Materials only available in the online version of record: machine-readable table

1. Introduction

Much of the light from star formation is absorbed by dust and reemitted in the infrared (IR; $\gtrsim$3 μm), affecting galaxy populations at all redshifts and especially in the range $z = 1$–4, where dust-obscured star formation dominates by factors 2–4 over the unobscured component, with nonnegligible effects in galaxies out to $z \sim 8$ (e.g., P. Madau & M. Dickinson 2014; C. M. Casey et al. 2018; R. Bouwens et al. 2020; J. A. Zavala et al. 2021; P. Dayal et al. 2022; F.-Y. Liu et al. 2025). Locally, galaxies show a wide range of IR properties, as they include different mixes of highly obscured, IR-bright regions and almost transparent, IR-faint ones.

The efforts to calibrate IR-based indicators of the dust-obscured star formation span several decades in time, starting with the galaxy surveys from the IRAS satellite, and continuing through recent years, as sensitivity and resolution increased. For as long, it has been clear that the IR emission is at best an imperfect tracer of the dust-obscured star formation. While stars form in dusty environments, at least in the local Universe, and young stars can therefore be considered prime sources of dust heating, the IR emission we observe in galaxies and in galaxy regions is from dust heated by stellar populations of all ages.

Because of the above, models predict that the calibration of the IR emission into a star formation rate (SFR) is age dependent, with lower calibration constants for population mixes that span longer star formation timescales (D. Calzetti 2013). The duration τ of star formation, and the star formation history (SFH) in general, affects the IR SFR calibrations by changing the bolometric luminosity, the shape of the UV–optical spectral energy distribution (SED) and the dust optical depth of galaxies and regions over time; for monochromatic IR SFR indicators, calibrations are also affected by the dependence of the effective dust temperature on mean stellar population age. Observationally, this has been handled in indirect ways, through either spectral decomposition of the IR SED (G. Helou 1986; C. J. Lonsdale Persson & G. Helou 1987; V. Buat & J. M. Deharveng 1988; D. A. Hunter et al. 1989; M. Rowan-Robinson & J. Crawford 1989; M. Sauvage & T. X. Thuan 1992; V. Buat & C. Xu 1996; R. A. M. Walterbos & B. Greenawalt 1996; A. Boselli et al. 2004; D. A. Dale et al. 2012) or spatial decomposition, when spatial information is available (D. Calzetti et al. 2005, 2007, 2010; G. J. Bendo et al. 2012; D. J. B. Smith et al. 2012; Y. Li et al. 2013; B. Magnelli et al. 2014; M. Boquien et al. 2016; N. Tomičić et al. 2019; B. Gregg et al. 2022; A. K. Leroy et al. 2023). The results yield a large range, ≈20%–70%, for the contribution of young star-forming regions to the IR emission in local galaxies, possibly linked to differences in the constituents of individual samples (G. Liu et al. 2011; Y. Li et al. 2013; M. Boquien et al. 2016; A. K. Leroy et al. 2023; D. Calzetti et al. 2024).

While the studies listed above have recognized the age dependence of IR SFR indicators and proposed ways to take them into account, explicit calibrations of the IR SFR as a function of star formation timescale have been scant (Y. Li et al. 2013; D. Calzetti et al. 2024). This has mainly been driven by limitations in the observations, especially in spatial resolution, since star formation is hierarchical and younger ages are associated with smaller scales in star-forming galaxies (e.g., Y. N. Efremov & B. G. Elmegreen 1998; R. de la Fuente Marcos & C. de la Fuente Marcos 2009; B. G. Elmegreen 2011, 2018; D. A. Gouliermis et al. 2015; K. Grasha et al. 2015, 2017a, 2017b; D. A. Gouliermis 2018; G. Shashank et al. 2025). Direct evidence for the existence of an age dependence in the IR SFR calibration exists in the Milky Way. Several authors have demonstrated that different SFR indicators yield a consistent value $\sim 2\ M_{\odot}\ \mathrm{yr}^{-1}$ for the Milky Way (L. Chomiuk & M. S. Povich 2011; I. Mendigutía et al. 2018; D. Elia et al. 2022; J. D. Soler et al. 2023); however, it is also clear that each indicator can only be used exclusively in the regime it applies. D. Elia et al. (2025) demonstrate that applying an IR SFR indicator calibrated for ∼kiloparsec-sized galaxy regions to the IR luminosity of Milky Way clumps yields a more than 1 order of magnitude underestimate of the Galaxy's SFR. This is understood because the galaxy-wide calibrations include (and correct for) the diffuse IR emission from the entire stellar population and not from just the <1 Myr old clumps. Now that the synergy between JWST and the Atacama Large Millimeter/submillimeter Array is providing samples of distant galaxies with both UV–optical and IR information, exploring the explicit age dependency of IR SFR indicators is becoming more necessary and urgent.

In this paper, we expand on the investigation presented in D. Calzetti et al. (2024) to quantify the relation between 21 μm dust emission and SFR at the scale of H II regions in two nearby galaxies: NGC 5194 and NGC 628. We also expand our analysis to include results, from Spitzer Space Telescope (Spitzer) MIPS/24 μm (G. H. Rieke et al. 2004) and other data, on larger, kiloparsec-sized regions and whole galaxies; we finally use models to reconcile the different IR SFR calibrations into a single, coherent picture.

Our first step is to focus on H II regions because the ionized gas traces young, massive stars and are usually easily identifiable units of recent star formation; hydrogen recombination lines probe ages < 6–7 Myr (C. Leitherer et al. 1999). The ionizing photon rate mainly probes the masses of these star formation units, but when averaged over a large number of H II regions of different masses, it becomes an accurate SFR indicator over that same timescale of ∼6 Myr. This sets the shortest timescale we can probe with our investigation, which it is sufficient to detect differences in the IR emission when compared with kiloparsec-sized galaxy regions or whole galaxies, since the latter probe crossing times of ≈100 Myr to gigayears.

D. Calzetti et al. (2024) already analyzed the H II regions in NGC 628, and we will be adding here those of NGC 5194. The main properties of NGC 5194 used in this paper are listed in Table 1, together with those of NGC 628. The two galaxies

Table 1
Properties of the Galaxies

Parameter	Units	NGC 5194	References[a]	NGC 628[b]
Distance	Mpc	7.55	(a)	9.3
Inclination	deg	22	(b)	9
R_{25}	arcsec (kpc)	336.6 (12.32)	(c)	314.2 (14.15)
$E(B-V)_{MW}$[c]	mag	0.031	(d)	0.06
M_{star}	$M_{\odot}$	2.3×10^{10}	(e)	9.9×10^{9}
SFR	$M_{\odot}$ yr^{-1}	6.7	(e)	3.2
$12 + \mathrm{Log(O/H)}$[d]	⋯	8.75	(f)	8.71
Gradient[e]	R_{25}	−0.27	(f)	−0.40
M_{dust}/M_{star}	⋯	4.5×10^{-3}	(g)	4.2×10^{-3}

Notes.
[a] References for the NGC 5194 parameters: (a) E. Sabbi et al. (2018), using the tip of the red giant branch; similar results are obtained by G. Csörnyei et al. (2023) and a slightly larger distance, 8.58 Mpc, by K. B. W. McQuinn et al. (2016); (b) D. Colombo et al. (2014), using CO emission; (c) G. de Vaucouleurs et al. (1991); (d) E. F. Schlafly & D. P. Finkbeiner (2011); (e) D. Calzetti et al. (2015); (f) D. A. Berg et al. (2020); (g) D. A. Dale et al. (2023).
[b] The parameters for NGC 628 are the same reported in D. Calzetti et al. (2024). We refer the reader to that work for the relevant references. The M_{dust}/M_{star} value for this galaxy is from D. A. Dale et al. (2023).
[c] Foreground Milky Way extinction.
[d] Central oxygen abundance. We adopt a solar oxygen abundance of $12 + \mathrm{Log(O/H)} = 8.69$, M. Asplund et al. (2009).
[e] Metallicity gradient as a function of galactocentric radius in units of R_{25}.

present both similarities and differences. NGC 5194 is slightly closer than NGC 628, and has a twice higher overall SFR, implying that it has a higher density of H II regions,[35] and is twice as massive. The two galaxies are both located a factor of a few above the main sequence of star formation (D. O. Cook et al. 2014; A. Renzini & Y.-j. Peng 2015), but their dust-to-stellar mass ratios fall along the local galaxy sequence (D. A. Dale et al. 2023). Both galaxies have a little over solar oxygen abundance in their center, and modest radial gradients (D. A. Berg et al. 2020). The region in common among the JWST mosaics in different bands of NGC 5194 extends to about 187″ from the center (0.556 R_{25} or 6.8 kpc), implying that the metallicity has decreased by only 0.15 dex at that point. We will, therefore, model the H II regions in NGC 5194 as having a single, ∼solar, metallicity value.

We concentrate on 21 μm (24 μm) as opposed to the shorter-wavelength dust emission features, as the latter are also sensitive to metallicity and ionization variations and dust carrier destruction (O. V. Egorov et al. 2023; A. Pedrini et al. 2024). The hydrogen recombination line Paα (1.8756 μm) is used as an unbiased SFR indicator, after it is corrected for dust attenuation using the archival Hubble Space Telescope (HST) Hα (0.6563 μm) imaging. As in D. Calzetti et al. (2024), we select H II regions that are bright enough, and thus massive enough, to minimize the effects of stochastic (random) sampling of the stellar initial mass function (IMF). This approach is different from the one utilized by F. Belfiore et al. (2023), who analyzed ∼20,000 H II regions in 19 nearby galaxies, but included faint, stochastic H II regions and did not account for diffuse IR emission in their analysis.

[35] The two galaxies have comparable areas as measured from R_{25}, see Table 1.

Table 2
NGC 5194 Imaging Data Sources

Telescope[a]	Instrument[b]	Filters[c]	Proposal ID[d]
JWST	NIRCam S + L	F150W, F187N, F200W, F444W	1783
JWST	MIRI	F2100W	3435
HST	ACS/WFC	F555W, F658N, F814W	10452

Notes.
[a] JWST (J. P. Gardner et al. 2023; J. Rigby et al. 2023).
[b] NIRCam S + L = NIRCam, short- and long-wavelength channels (M. J. Rieke et al. 2005, 2023); MIRI (G. H. Rieke et al. 2015); Advanced Camera for Surveys (ACS) Wide Field Channel (WFC; M. Sirianni et al. 2005).
[c] Filter names. The F187N and the F658N narrowband filters are centered on the hydrogen recombination lines Paα(1.8756 μm) and Hα(0.6563 μm) respectively.
[d] Identification of the GO program that obtained the images: JWST/GO-1783 (JWST-FEAST), PI: Adamo; JWST/GO-3435 (JWGT), PIs: Sandstrom and Dale; and HST GO 10452, PI: Beckwith, Hubble Heritage Team.

This paper is organized as follows: Section 2 presents the data used in this analysis, Section 3 describes the source identification and measured properties, and Section 4 presents the main results for NGC 5194 first and then combined with the H II regions of NGC 628. Section 5 discusses the results, also in comparison with published samples of galaxies and of ∼kiloparsec-sized galaxy regions, providing H II region-to-galaxy calibrations for IR SFRs. Conclusions and recommendations on the use of these IR SFR calibrations are given in Section 6.

2. NGC 5194 Imaging Data and Processing

The galaxy NGC 5194 is one of six targets of the Cycle 1 JWST program 1783 (JWST Feedback in Emerging Extragalactic Star Clusters (JWST-FEAST); PI: A. Adamo) and the target of the Cycle 2 JWST Treasury program 3435 (The JWST Whirlpool Galaxy Treasury (JWGT); PIs: K. Sandstrom and D. Dale). Both programs have observed the galaxy with both NIRCam (M. J. Rieke et al. 2005, 2023) and MIRI (G. H. Rieke et al. 2015), obtaining mosaics in complementary filters across the two instruments, and covering the wavelength range 1.1–21 μm. Mosaics in NIRCam were processed through the JWST pipeline version 1.12.5 (2023 December release) using the Calibration Reference Data System (CRDS) context "jwst_1174.pmap," while the MIRI mosaics were processed through the JWST pipeline version 1.13.4 (2024 February release) using the CRDS context "jwst_1241.pmap."[36] The mosaics utilized in this work are listed in Table 2 together with the program number they originated from: we use the NIRCam mosaics from JWST-FEAST and one MIRI (21 μm) mosaic from JWGT. A small rotation between the fields view view of the NIRCam mosaics and the MIRI mosaic, both centered on the galaxy's center, reduces the effective overlap area to $\sim 2' \times 5.'7$, or $4.4 \times 12.6\,\mathrm{kpc}^2$. Furthermore, the NIRCam mosaics have common pixel scale of 0.″04 pixel^{-1} and are in units of Jy pixel^{-1}, while the MIRI mosaic has pixel scale of 0.″11 pixel^{-1} and is in units of MJy sr^{-1}.

[36] https://jwst-pipeline.readthedocs.io/en/latest/jwst/user_documentation/reference_files_crds.html

HST/ACS/WFC imaging of NGC 5194 was retrieved from the Mikulski Archive for Space Telescopes (MAST) archive at the Space Telescope Science Institute.[37] The HST imaging is a 2×3 pointing mosaic covering the entire bright area of NGC 5194 and its companion NGC 5195 obtained by HST GO 10452 (PI: S. Beckwith), as part of the HST image release program by the Hubble Heritage Team. The HST mosaic coverage is sufficiently extended to completely include the JWST mosaics. The JWST-FEAST team reprocessed the archival images, resampling them to a pixel scale of 0.″04 pixel^{-1}. Flux calibration is in units of counts s^{-1}, which we convert to physical units using the PHOTFLAM image header keywords. Of the four ACS/WFC filters available for this galaxy from the Heritage program, we only utilize three: F555W, F658N, and F814W, as will be discussed below. See Table 2 for details on the telescope, instruments, and filters for the HST mosaics.

The F2100W mosaic has the lowest resolution among all images used in this work: the MIRI F2100W point-spread function (PSF) has an FWHM of 0.″674, which subtends about 25 pc at the distance of NGC 5194. This is comparable to or larger than the size of a single H II region (see next section); thus, we will be relying on the shorter-wavelength, higher angular resolution mosaics to identify H II regions that are ionized by individual star clusters. The short-wavelength NIRCam mosaic in the F150W filter has a PSF FWHM $= 0.''05$; the PSF of F200W has a similar FWHM $= 0.''066$; and F187N has FWHM $= 0.''061$. At the distance of NGC 5194, the short-wavelength NIRCam PSF corresponds to 1.8–2.4 pc, implying that compact star clusters, which have characteristic radius $\sim$3 pc (J. E. Ryon et al. 2015, 2017; G. Brown & O. Y. Gnedin 2021), are marginally resolved.

Emission line maps are derived from the narrowband mosaics: NIRCam F187N centered on the Paα line emission ($\lambda = 1.8789$ μm at the fiducial redshift $z = 0.001745$)[38] and ACS/WFC F658N centered on the Hα + [N II] doublet line emission ($\lambda = 0.6559$, 0.6574, and 0.6595 μm at $z = 0.001745$). The interpolation between F150W and F200W is used to produce a stellar continuum image to subtract from F187N. Since F200W contains the Paα emission, we iteratively subtract the line from this filter, using the procedure described in M. Messa et al. (2021) and D. Calzetti et al. (2024), until differences between two subsequent iterations are $\lesssim$0.1% in flux. The interpolation between F555W and F814W is used to produce a stellar continuum image to subtract from F658N. The F555W filter includes [O III] (0.5007 μm) line emission, but D. Calzetti et al. (2024) showed that in metal-rich galaxies this contribution is small, affecting the interpolated stellar continuum by $\lesssim$1.5%. The F658N line emission is then corrected for the [N II] contribution, using [N II]/H$\alpha = 0.6$ for the sum of the two [N II] components (J. Moustakas & R. C. Kennicutt 2006; R. C. J. Kennicutt et al. 2008). As discussed in Section 1 (see also Table 1), the metallicity gradient is $\leqslant$0.15 dex within the JWST footprint; we thus, neglect [N II]/Hα variations and only include a 6% uncertainty on the [N II]/Hα measurement in our error propagation (J. Moustakas & R. C. Kennicutt 2006). The final line flux maps in Hα and Paα are derived by multiplying the continuum-subtracted mosaics by the respective bandwidths (0.00875 μm for F658N[39] and 0.024 μm for F187N)[40] and by correcting for the filter transmission curve value at the galaxy's redshift.

3. Source Selection, Photometry, and Physical Quantities

For the source selection, we adopt the same approach and criteria as D. Calzetti et al. (2024). The Paα and 21 μm images are inspected visually to isolate sources that are compact both in Paα and in stellar continuum (from the F814W mosaic), are detected with a signal-to-noise ratio (S/N) $\gtrsim 5$ at 21 μm and S/N $\gtrsim 3$ in both Paα and Hα, and are spatially coincident in the two bands to better than the 21 μm PSF FWHM. In this context, a "compact source" is a source that displays a single peak in the line emission image within the photometric aperture (see below) and has a colocated stellar continuum source that shows either a single peak or clustered emission; the latter are sources showing multiple peaks immersed in a common, fainter emission region (likely low-mass, unresolved stars). At the resolution of our images (Section 2) these sources are likely to be individual star clusters or compact associations (A. Adamo et al. 2017). All sources that appear extended or shell-like in the Paα image are excluded from further consideration, as these are expected to correspond to evolved (older than $\sim$6 Myr) H II regions (B. C. Whitmore et al. 2011). We further require that the sources are sufficiently separated from each other that adjacent photometric apertures do not overlap more than 10% to ensure independent photometric measurements. As will be discussed later, requiring *both* Paα and Hα to be detected with S/N $\gtrsim 3$ imposes a luminosity-dependent upper limit on the highest value of dust extinction a region can have; however, this upper limit is sufficiently above the bulk of the sources' measurements to not represent a limitation to this analysis. Our selection is incomplete for sources that are faint in all three Paα, Hα, and 21 μm images; this will not affect our analysis, because we implement a luminosity cut at the faint end to remove sources that are affected by stochastic sampling of the stellar IMF (see Section 4). A total of 254 sources meeting the above criteria are found across the JWST footprint of NGC 5194 (Figure 1).

For the photometry, we deviate from D. Calzetti et al. (2024) in that we select a smaller aperture radius, 0.″7, which corresponds to about 26 pc at the distance of NGC 5194, instead of the radius of 1.″4 that we used for NGC 628 (corresponding to a physical scale of 63 pc in this galaxy). The reason for the different choice is that H II regions are more densely packed in NGC 5194 than in NGC 628, requiring a smaller aperture size to separate adjacent regions. Although the de-projected aperture corresponds to an ellipse with semimajor and semiminor axes of 28 pc and 26 pc, respectively, we will continue to treat the apertures as round, under the assumption that H II regions can be basically considered spherically symmetric. A concern is whether the small aperture may be missing significant portions of the ionized gas emission surrounding each star cluster. For our sources, the largest Strömgren radius is about 26–27 pc (D. E. Osterbrock & G. J. Ferland 2006) for uniform density, when using the electron densities from K. V. Croxall et al.

[37] https://archive.stsci.edu/.
[38] From NASA Extragalactic Database (NED).
[39] https://etc.stsci.edu/etcstatic/users_guide/appendix_b_acs.html
[40] https://jwst-docs.stsci.edu/jwst-near-infrared-camera/nircam-instrumentation/nircam-filters

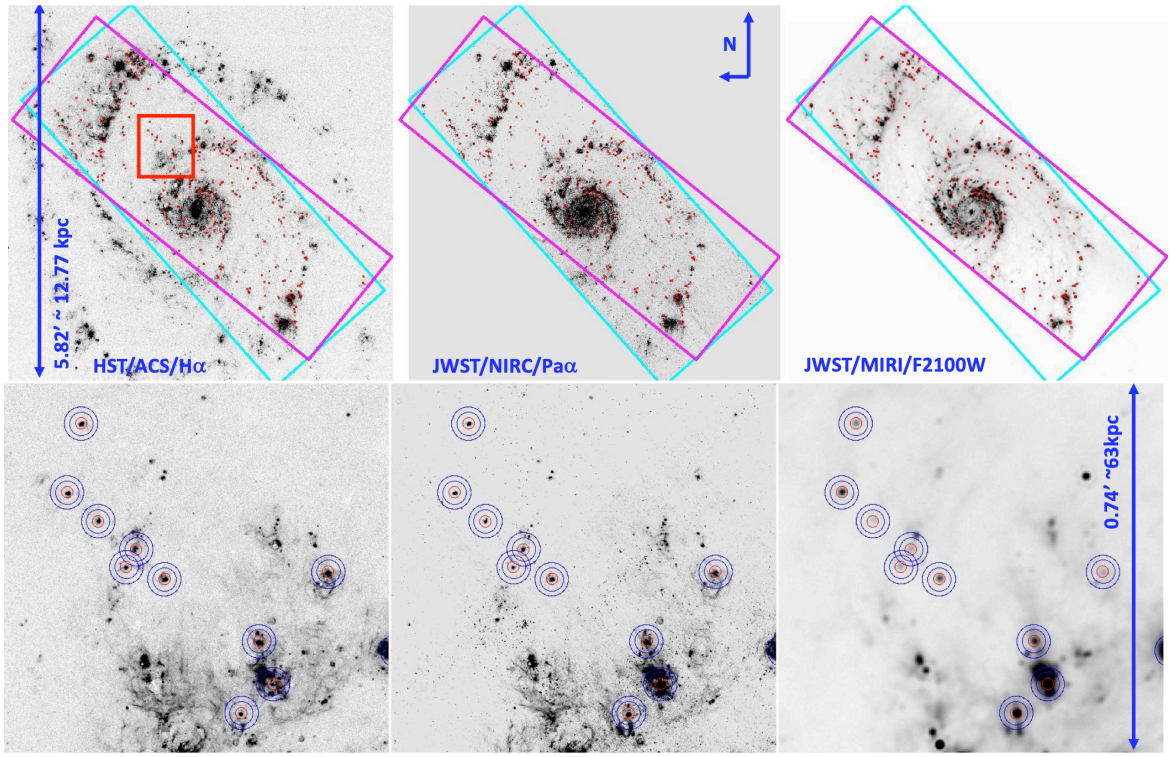

Figure 1. Top row: the 254 sources emitting in Hα, Paα, and 21 μm are identified with red circles on the JWST and HST mosaics of NGC 5194 in the stellar-continuum-subtracted HST/ACS Hα image (left), JWST/NIRCam Paα image (center), and JWST/MIRI F2100W image (right), see Section 2. The NIRCam footprint and the MIRI footprint are shown as cyan and magenta rectangles, respectively, on all three panels. The radius of the circles matches the photometric aperture used in this study, 0.″7, or ~26 pc. North is up, east is left. Bottom row: a detailed look at the images above, in the same order (Hα, Paα, and 21 μm, respectively). The double blue circle around each region shows the size of the annulus used for the local background subtraction (1.″4 inner radius with 0.″6 width). The location of this region is drawn on the top-row Hα image with a red rectangle.

(2015), $n_e \sim$ 70–200 cm^{-3} along the JWST mosaic's strip. Thus, our apertures are well matched to the largest Strömgren sphere we sample, alleviating any concern of missed ionizing flux.

The photometric apertures are centered on the centroid of the 21 μm sources. In a few cases, the wings of the nebular emission are sufficiently bright that it is desirable to center the aperture on the Paα peak, so to capture as much as possible the source's ionized gas emission. In an additional two dozen cases, the regions are sufficiently crowded that the apertures need to be moved slightly to avoid >10% overlap between adjacent apertures. These can result in aperture centers that are slightly offset relative to the 21 μm peak. For all off-center cases, we measure the impact of the de-centering on the 21 μm photometry and find that, except for six cases, the impact is smaller than the measurement uncertainty. The six impacted sources (all to <20% level) are located in crowded regions and their photometry may be affected by the wings of neighboring sources; for these cases, we carry additional uncertainty in the 21 μm photometry. Photometry is obtained with local background subtraction, with the background measured in an annulus with inner radius = 1.″4 and outer radius = 2.″0 (blue circles in Figure 1, bottom panels). The size of the background annulus is twice as large as the radius of the photometric aperture, to exclude the majority of the emission in the wings of the 21 μm PSF: 1.″4 corresponds to 5σ for this PSF, and only 17% of the 21 μm flux is contained outside of it. The value of the local background around each source is the mode of the pixel value distribution after iterative σ clipping.

Aperture corrections are calculated for Paα, Hα, 21 μm, and F444W, the latter used to assess the stellar continuum contribution to the 21 μm band. Simulated flight PSFs are retrieved from the STScI Box repository,[41] and growth curves are generated to emulate our photometric approach. Aperture corrections to an infinite aperture are 7% for F187N (we adopt the same for F658N, as the PSFs are similar), 9% for F444W, and 41% for 21 μm. The 21 μm correction, which is the largest applied to our photometry, agrees with that derived from the in-flight PSF to within 1% (D. Dicken et al. 2024; M. Libralato et al. 2024). The aperture corrections are applied to the narrowband filter photometry after removal of the underlying stellar continuum.

Stellar continuum is removed from the 21 μm measurements by rescaling the F444W photometry to the central wavelength of the MIRI F2100W filter and then subtracting it from the 21 μm flux, using the approach described by D. Calzetti et al. (2024): $f(21)_{\rm dust} = f(21) - 0.046\ f(444)$, where the flux densities are in units of Jy. This method assumes that the F444W filter is dominated by stellar emission, and both dust attenuation and emission are negligible. The latter is not strictly correct, as the dust emission contribution to F444W can be substantial, especially in star-forming regions (S. E. Meidt et al. 2012). However, even under the strict assumption that F444W is entirely due to stellar emission, the stellar contribution to the 21 μm emission is <2% for all selected sources. Thus, the 21 μm emission is, for all practical purposes, not affected by stellar contamination. Local

[41] https://stsci.app.box.com/v/jwst-simulated-psf-library

Table 3
Source Location, Luminosity, and Derived Quantities for the H II Regions in NGC 5194

ID (1)	R.A.(2000), Decl.(2000) (2)	Log[L(Hα)] (3)	Log[L(Paα)] (4)	Log[L(21)] (5)	Log[EW(Paα)] (6)	$E(B-V)$ (7)
1	13:29:52.1548, +47:12:44.750	38.382 ± 0.040	37.896 ± 0.033	40.097 ± 0.054	2.863 ± 0.052	0.549 ± 0.070
2	13:29:52.0449, +47:12:47.270	38.481 ± 0.039	37.901 ± 0.033	39.952 ± 0.055	3.254 ± 0.063	0.421 ± 0.069
3	13:29:52.3785, +47:12:38.550	37.706 ± 0.054	37.682 ± 0.037	40.037 ± 0.054	3.410 ± 0.084	1.174 ± 0.088
4	13:29:51.1734, +47:12:45.511	37.976 ± 0.047	37.687 ± 0.037	39.911 ± 0.055	3.340 ± 0.079	0.816 ± 0.080
5	13:29:51.0399, +47:12:40.551	37.478 ± 0.063	37.561 ± 0.039	39.985 ± 0.054	3.073 ± 0.073	1.318 ± 0.100
6	13:29:55.0593, +47:12:20.546	37.716 ± 0.054	37.250 ± 0.048	39.150 ± 0.068	2.874 ± 0.084	0.577 ± 0.097
7	13:29:55.0439, +47:12:32.066	37.045 ± 0.088	36.948 ± 0.062	39.250 ± 0.065	2.798 ± 0.105	1.075 ± 0.145
8	13:29:54.6710, +47:12:35.547	36.828 ± 0.106	37.287 ± 0.047	39.667 ± 0.058	2.632 ± 0.071	1.825 ± 0.156
9	13:29:54.6904, +47:12:23.787	37.094 ± 0.084	37.057 ± 0.056	39.133 ± 0.068	2.831 ± 0.097	1.156 ± 0.136
10	13:29:54.8360, +47:12:40.666	37.354 ± 0.068	37.007 ± 0.059	38.924 ± 0.076	2.785 ± 0.099	0.737 ± 0.122

Notes. Table 3 is published in its entirety in the online article. A portion is shown here for guidance regarding its form and content. (1) The identification number of the source. (2) R.A. and decl. in J2000 coordinates. (3)–(5) Logarithm of the luminosity of each source at the indicated wavelength, in units of erg s^{-1}. The photometry is measured in circular apertures with 0.″7 radius on the plane of the sky. The Hα and Paα luminosities are corrected for Milky Way foreground extinction. See text for more details. (6) The logarithm of the EW of Paα, in Å units, calculated from the ratio of the emission line flux to the stellar continuum flux density. (7) The color excess, $E(B-V)$, in mag, derived from the Hα/Paα luminosity ratio.

(This table is available in its entirety in machine-readable form in the online article.)

background subtraction removes the diffuse dust emission from the general stellar population in the galaxy, thus eliminating contributions that are unrelated to the dust heating by the H II region. The flux density at 21 μm is then multiplied by the frequency to convert it to flux, which is standard for SFR measurements, and then converted to a luminosity using our adopted distance for NGC 5194 (Table 1). The 5σ limit for Log[L(21)] is 37.62,[42] in units of erg s^{-1}.

Line fluxes for the nebular emission are derived by applying the procedure described in Section 2 to the photometric measurements. For the H II regions, the stellar continuum subtraction corrects also for the underlying stellar absorption, which can lead to underestimates of the true line emission if not removed, while the local background subtraction removes the diffuse contribution from photon leakage and from scattered light coming from other regions. Both Hα and Paα fluxes are corrected for foreground Milky Way extinction (Table 1) and then converted to luminosities. The 3σ detections limits are 35.65 and 35.54 in erg s^{-1} units for Log[L(Hα)] and Log[L(Paα)], respectively.

Additional quantities used in this work are the equivalent width (EW) of Paα and the color excess $E(B-V)$. The EW is the ratio of the line luminosity to the luminosity density of the interpolated stellar continuum, in units of Å. The color excess is derived from the observed line ratio Hα/Paα, adopting Case B recombination and an intrinsic ratio of 7.82. This ratio is appropriate for metal-rich sources ($T_e = 7000$ K and $n_e = 100$ cm^{-3}; D. E. Osterbrock & G. J. Ferland 2006). We use the extinction curve extended to the JWST filters by K. Fahrion & G. De Marchi (2023) for 30 Doradus: κ(Hα) = 2.53 and κ(Paα) = 0.678, where $\kappa(\lambda) = A(\lambda)/E(B-V)$ is the ratio of the attenuation to the color excess. Although our sources are in a more metal-rich environment than the LMC, they are all H II regions like 30 Doradus, thus we assume the curve by K. Fahrion & G. De Marchi (2023) to be appropriate for our case; however, we adopt $R_V = 3.1$ as appropriate for metal-rich galaxies like the Milky Way (E. L. Fitzpatrick et al. 2019). Dust attenuation-corrected luminosities in the nebular lines are derived under the assumption of foreground dust, as $L(\lambda)_{\rm corr} = L(\lambda)10^{0.4E(B-V)\kappa(\lambda)}$, where $L(\lambda)$ and $L(\lambda)_{\rm corr}$ are the observed and attenuation-corrected luminosities in units of erg s^{-1}, respectively, and $\kappa(\lambda)$ is the dust attenuation curve. Given the small spatial scale sampled by our measurements, we assume the same dust attenuation values for emission lines and stellar continuum, implying that EWs are not affected by attenuation corrections. Table 3 lists for each source the ID, location on the sky in R.A.(2000) and decl.(2000), observed luminosity in Hα, Paα, and 21 μm, the EW in Paα, and the color excess $E(B-V)$.

[42] Log = $\log_{10}$ in this work.

4. Analysis and Results

4.1. Properties of the Emission Line Regions

The H II regions in NGC 5194 show many characteristics that are similar to the H II regions in NGC 628 (D. Calzetti et al. 2024). The observed Hα is underluminous relative to the Paα when using as reference the intrinsic ratio L(Hα)/L(Paα) = 7.82 discussed in the previous section, implying that almost all regions have some dust, with the only exception being the faintest ones (Figure 2, left). In addition, the lower envelope to the data for the color excess $E(B-V)$ increases for increasing luminosity (Figure 2, right), i.e., more luminous H II regions tend to be dustier than less luminous ones, with a minimum $E(B-V)_{\rm min} \sim 0.5$ mag at L(Paα) $\sim 10^{38}$ erg s^{-1}. Visual inspection of the Hα image indicates that this is not the result of biased selection: no regions are missing from our sample across the area in common between the HST and JWST mosaics that are at the same time bright in Hα and low in dust attenuation, while also satisfying both our Paα and 21 μm selection criteria. As already mentioned above, our 3σ limit in line detection introduces a luminosity-dependent upper limit to $E(B-V)$, shown as a gray slanted area in Figure 2 (right panel). The majority of our regions are not affected by this limit, although we cannot exclude the presence of even dustier regions. However, since the distribution of the selected regions clusters around a locus well below the upper limit in $E(B-V)$, we will assume that our sample is not missing a significant number of very dusty regions.

EW(Paα) marks a clear trend of decreasing values with decreasing luminosity of the attenuation-corrected Paα

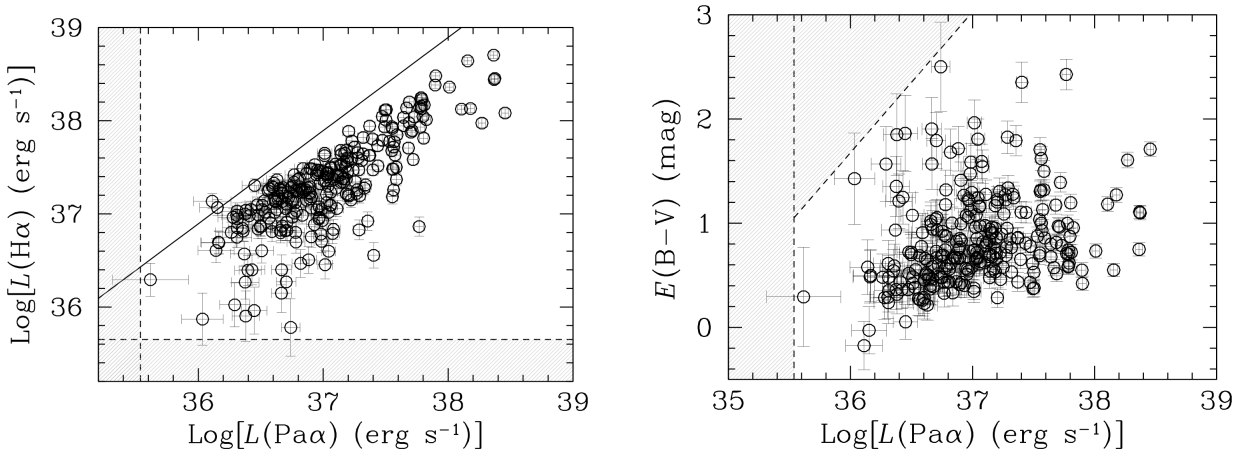

Figure 2. The observed luminosity in Hα (left panel) and the color excess $E(B-V)$ derived from the observed nebular luminosities (right panel) as a function of the observed Paα luminosity for the 254 regions identified in the JWST + HST mosaics of NGC 5194. All quantities are corrected for foreground extinction from the Milky Way (Table 1). The data are shown as black circles with their 1σ uncertainties. The continuous black line in the left panel marks the expected location of luminosities of the two emission lines for our adopted line ratio of 7.82 and with zero dust attenuation. The gray-shaded regions mark the areas below 3σ detection.

(Figure 3, left). The maximum EW and $L(\mathrm{Pa}\alpha)_{\mathrm{corr}}$ are consistent with the expected values for an H II region powered by an $\sim$3 Myr old, 3×10^5 $M_\odot$ star cluster. However, the trend is overall inconsistent with the expected track of aging H II regions (magenta dotted line in Figure 3, left), since the majority of the data are located above this track. The model that best describes the observations is a modification of the model used to explain a similar trend in NGC 628 (D. Calzetti et al. 2024): the clusters powering the H II regions are all roughly the same age, $\lesssim$5 Myr, but have decreasing mass when going from high to low EW and are immersed in a constant-luminosity, nonionizing background stellar field.

The models used for NGC 628 are shown as blue lines in Figure 3 (left), and they underestimate the EW of the H II regions in NGC 5194 at any given luminosity, with the exception of the brightest regions. The reason for this discrepancy is that there are differences in the properties and treatment of the two galaxies: the photometric aperture used for NGC 5194 is 4 times smaller in angular area than that used in NGC 628 and the median stellar field surrounding H II regions in NGC 5194 has about a 30% higher surface brightness than in NGC 628. When these two differences are included, the resulting model accounts reasonably well for the mean observed trend (red continuous line) of EW versus $L(\mathrm{Pa}\alpha)_{\mathrm{corr}}$. The observed scatter in the background stellar field, corresponding to factors of -3 and $+5$ (red dashed lines), is also consistent with the width of the distribution of the field's luminosity values. All regions have EWs consistent with H II regions younger than 6 Myr; the 6 Myr model track (cyan line) is located below the locus of the data, and therefore underestimates the observations. The youth of our H II regions is consistent with our selection criteria of regions with compact ionized gas emission, in agreement with B. C. Whitmore et al. (2011) and S. Hannon et al. (2022).

The seven brightest H II regions, with $L(\mathrm{Pa}\alpha)_{\mathrm{corr}} \gtrsim 10^{38.4}$ erg s^{-1}, mark the asymptotic behavior of the EW with $L(\mathrm{Pa}\alpha)$ at high luminosity. Their values, Log(EW) $\sim$ 3.19–3.55, are consistent with either a 3–4 Myr old massive cluster (see above) with no ionizing photon loss or a younger, $\sim$1–2 Myr, cluster about 4 times less massive and with $\approx$50% ionizing photon loss. Recent results (A. Pedrini et al. 2025) indicate that current models may not account completely for the presence of pre-main-sequence stars, which leads to an underestimate of the true stellar continuum around the Paα emission line by 0.12–0.2 dex. The higher continuum corresponds to an identical downward shift in EW(Paα) and the ages of the brightest clusters would be closer to $\sim$2 Myr. If we assume $\lesssim$50% of ionizing photon loss, there are at least two possible sources for this, as already discussed by D. Calzetti et al. (2024). One possibility is photon leakage from the H II regions, which E. W. Pellegrini et al. (2012) determined to correlate with source luminosity, being larger for brighter sources. The second possibility is direct absorption of ionizing photons (prerecombination cascade) by dust, which is also consistent with our data, as more luminous H II regions are also dustier on average (Figure 2, right, and Figure 3, right). According to the models of M. R. Krumholz & C. D. Matzner (2009) and B. T. Draine (2011), there is a maximum theoretical value of 20%–70% ionizing photons that can be directly absorbed by dust in the brightest and dustiest H II regions depending on physical conditions (see also A. K. Inoue et al. 2001; M. A. Dopita et al. 2003). Our brightest regions, with $L(\mathrm{Pa}\alpha)_{\mathrm{corr}} \gtrsim 10^{38.4}$ erg s^{-1}, which corresponds to an ionizing photon rate $Q_o \gtrsim 1.4\times10^{51}$ s^{-1}, and $E(B-V)\gtrsim1$ mag, satisfy the conditions for such high level of direct dust absorption.

The color excess $E(B-V)$ shows a general trend of higher values for larger $\mathrm{Pa}\alpha_{\mathrm{corr}}$ luminosities (Figure 3, right). For reference, $E(B-V)=1$ mag suppresses the Hα emission by a factor of $\sim$10 and the Paα by a factor of $\sim$1.9. The observed trend is very similar to the one D. Calzetti et al. (2024) observed in NGC 628 (magenta points in Figure 3, right): there appears to be a lower envelope to the color excess of H II regions, with a lower limit that increases with luminosity. The $E(B-V)$ lower envelope is well described by the model of T. Garn & P. N. Best (2010, red line), which these authors derived for the mean extinction of galaxies, but seems to apply well to describe the lower boundary to the extinction of H II regions as a function of luminosity. The trend, however, is not limited to the lower envelope: brighter regions have larger values of the color excess on average, although the scatter

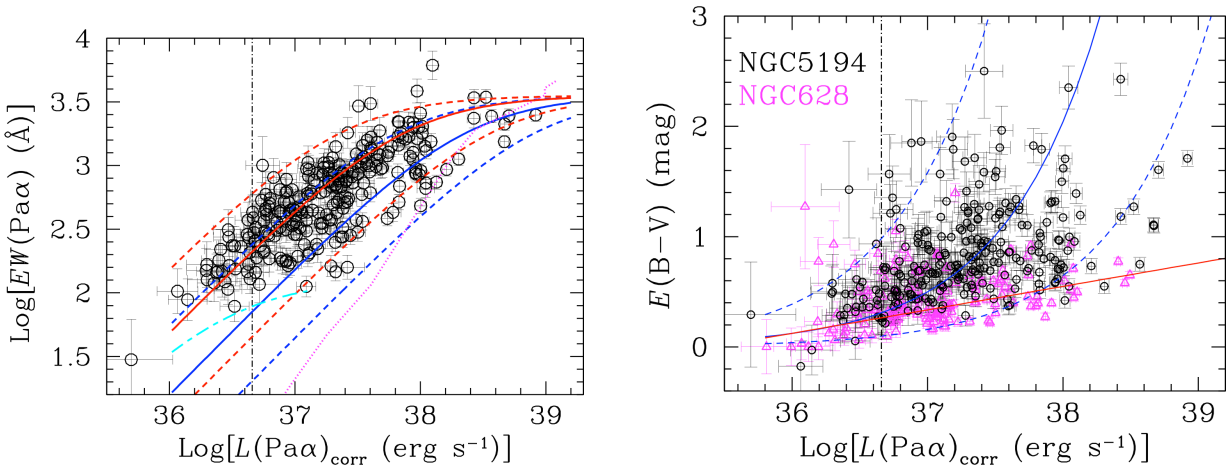

Figure 3. EW(Paα) (left panel) and the color excess $E(B-V)$ (right panel) as a function of the attenuation-corrected luminosity in Paα for the H II regions in NGC 5194. The data are shown as black circles, with their 1σ uncertainties. The right panel includes the data for NGC 628 as magenta triangles, with their 1σ uncertainties. Both panels show as a vertical black dotted–dashed line the expected Paα luminosity of a 4 Myr old, 3000 $M_\odot$ cluster, the lower-end luminosity limit in our analysis to mitigate stochastic IMF sampling effects (M. Cerviño et al. 2002). Left: the magenta dotted line shows the EW(Paα) model track of an H II region of constant mass $\sim 2\times10^5\,M_\odot$ with increasing age from 1 Myr (top right) to 10 Myr (bottom left). The red continuous line is the model track for a constant age, 3 Myr old, H II region of decreasing mass, from $\sim3\times10^5\,M_\odot$ down to $\sim2\times10^2\,M_\odot$, immersed in a constant-luminosity nonionizing stellar field, with a scatter of factors of −3 and +5 (higher and lower red dashed lines, respectively) about the mean trend. The cyan line is the same track, but for a 6 Myr old H II region. The blue lines are the tracks for NGC 628, from D. Calzetti et al. (2024), using the same model but with a larger photometric aperture (continuous line for the mean trend and dashed lines for the scatter). Right: the two empirical relations shown are from D. Calzetti et al. (2007) for ∼0.5 kpc star-forming regions (blue solid line for the mean trend and dashed lines for the 90th percentile) and from T. Garn & P. N. Best (2010) for galaxies (red continuous line).

increases with luminosity. D. Calzetti et al. (2007) derived an empirical fit for ∼kiloparsec galaxy regions together with the 90% scatter about the mean relation (see also Equation (B2) in Appendix B); those authors' fit is consistent with the trend observed for our H II regions and their 90 percentile lines bracket our data reasonably well (blue continuous and dashed lines).

Both panels in Figure 3 mark the expected Paα luminosity of a 4 Myr old cluster with a mass of 3000 $M_\odot$ as a vertical dotted–dashed line, corresponding to $L(\mathrm{Pa}\alpha)_{\rm corr}=10^{36.66}$ erg s^{-1}. We select this luminosity as the lower limit we consider in our analysis, since H II regions powered by lower-mass clusters are affected by stochastic sampling of the IMF (M. Cerviño et al. 2002). For those low-mass clusters, measurements of the ionizing photon rate are no longer a faithful representation of the massive star end of the IMF; the IMF is not fully sampled and the number of massive stars is randomly drawn from its distribution. With this luminosity limit, the remaining sample of 225 H II regions spans a little over 2 orders of magnitude in luminosity, which is sufficient to relate it to the 21 μm emission.

4.2. Properties of the Mid-infrared Emission and Calibration of the Star Formation Rate Indicators

The 21 μm luminosities of the H II regions in NGC 5194 are tightly correlated with the extinction-corrected Paα luminosities, similarly to what was found in NGC 628 (D. Calzetti et al. 2024) and other galaxies (F. Belfiore et al. 2023). The left panel of Figure 4 shows $L(21)$ as a function of $L(\mathrm{Pa}\alpha)_{\rm corr}$ for the H II regions in NGC 5194 and NGC 628, with the best fits to the two sets shown both separately and combined together. The best-fit line to the logarithm of the luminosities for NGC 5194, for the 225 regions which are above the stochastic IMF sampling limit $L(\mathrm{Pa}\alpha)_{\rm corr}=10^{36.66}$ erg s^{-1}, is

$$\mathrm{Log}[L(21)] = (1.17\pm0.02)\,\mathrm{Log}[L(\mathrm{Pa}\alpha)_{\rm corr}] - (4.51\pm0.90), \quad (1)$$

with scatter = 0.09 dex. We use the LINMIX package,[43] which applies a hierarchical Bayesian approach to linear regression (B. C. Kelly 2007), for all fits in this work. The reported best-fit parameters are the averages between the y versus x and x versus y relations, to mitigate the impact of the $L(\mathrm{Pa}\alpha)_{\rm corr}=10^{36.66}$ erg s^{-1} limit. Still used deterministic approaches to linear fitting, like the FITEXY (W. H. Press et al. 1992) and the ordinary least squares bisector (T. Isobe et al. 1990) algorithms, yield a similar slope, 1.18, but with significant smaller uncertainties, which have been shown to underestimate the true scatter in the data. The superlinear slope (slope > 1 in log–log space) can be attributed to several mechanisms, two already discussed in Section 4.1: photon leakage out of H II regions and direct dust absorption of ionizing photons, both of which affect bright regions more than faint ones. A third mechanism, which is likely to account for the majority of the effect is the fact that lower-luminosity H II regions tend to be less extincted than brighter ones (Figure 3, right), implying that a larger fraction of the ionizing and nonionizing photons at low luminosities emerge unaffected by dust attenuation and are not captured by the 21 μm luminosity. A fourth mechanism postulates that higher-luminosity H II regions produce "hotter" IR SEDs, which would increase the fraction of 21 μm emission relative to the total IR emission. This has been observed, with large scatter,

[43] The Python version of LINMIX used in this work can be found at https://github.com/jmeyers314/linmix.

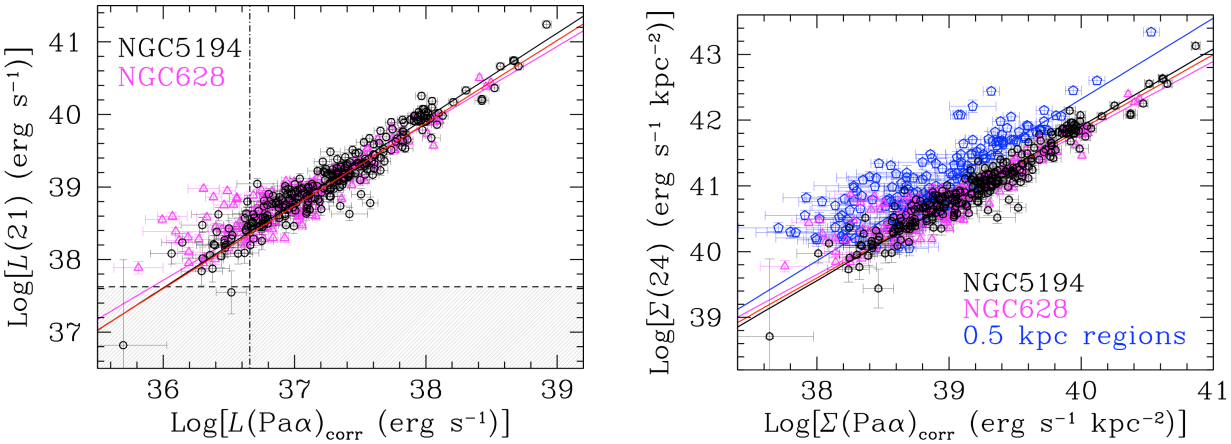

Figure 4. Left: the luminosity at 21 μm, $L(21)$, as a function of the attenuation-corrected luminosity at Paα for the 254 line-emitting regions in NGC 5194 (black circles, this work) and the 143 regions in NGC 628 (magenta triangles, D. Calzetti et al. (2024), with 1σ uncertainties. The horizontal dashed line and gray region show the location of the 5σ threshold at 21 μm in NGC 5194. The black and magenta lines show the best fits through the data with Paα luminosity above the IMF sampling limit (vertical dotted–dashed line) for the two galaxies separately, while the red line is for the data from the two galaxies combined. Right: the luminosity surface density at 24 μm, $\Sigma(24)$, as a function of the attenuation-corrected luminosity surface density at Paα for the same H II regions in NGC 5194 (black circles) and NGC 628 (magenta triangles), also with 1σ uncertainties, after converting the luminosity at 21–24 μm. The solid lines indicate the fits through the H II regions using the same color scheme as the left panel. The data for the luminosity surface densities of 160 ~0.5 kpc regions at ~solar metallicity from D. Calzetti et al. (2007) are shown as blue pentagons with the best linear fit from those authors marked as a blue line.

both in H II regions (M. Relaño et al. 2013) and in galaxies (G. H. Rieke et al. 2009; D. Calzetti et al. 2010).

The slope of 1.17 for the H II regions in NGC 5194 (Equation (1)) is slightly steeper than the one found for those in NGC 628 of 1.07 ± 0.03. The small, $<3\sigma$ difference between the two slopes can be accounted for by the presence of brighter H II regions in NGC 5194, which extend to a factor of ~3 higher luminosities than in NGC 628 and, for the reasons discussed above, steepens the slope. The difference in the slopes of the two sets of H II regions reduces to about 2σ, when fit over the same range of luminosities. In addition, the locus of the H II regions from the two galaxies largely overlaps (Figure 4), and we derive a combined relation for the 21 μm luminosity for the 336 H II regions (225 from NGC 5194 and 111 from NGC 628) that are above our adopted limit for stochastic sampling of the IMF:

$$\mathrm{Log}[L(21)] = (1.14 \pm 0.02)\mathrm{Log}[L(\mathrm{Pa}\alpha)_{\mathrm{corr}}] - (3.44 \pm 0.76), \quad (2)$$

with scatter = 0.09 dex. This fit has, as expected, a slope that is intermediate between the individual ones of the two galaxies, as is shown in red in Figure 4 (left).

Using $L(\mathrm{Pa}\alpha)_{\mathrm{corr}}$ as a reference SFR indicator (R. C. Kennicutt & N. J. Evans 2012), we derive an SFR calibration using the 21 μm luminosity:

$$\mathrm{SFR}(21)(M_\odot \mathrm{yr}^{-1}) = 4.44^{+2.91}_{-2.68} \times 10^{-38} L(21)^{0.877 \pm 0.015} \quad \text{for} \quad 10^{38} \lesssim L(21) \lesssim 2 \times 10^{41}. \quad (3)$$

The JWST 21 μm luminosities can be converted to Spitzer/MIPS 24 μm equivalents using the relation derived by D. Calzetti et al. (2024) for NGC 628: $\mathrm{Log}L(24) = \mathrm{Log}L(21) - 0.057$. Given the proximity in wavelength between the two IR luminosities, we do not expect major variations to this relation between NGC 628 and NGC 5194 and small variations have a negligible impact on the overall picture. We thus derive also an SFR calibration for the 24 μm emission:

$$\mathrm{SFR}(24)(M_\odot \mathrm{yr}^{-1}) = 4.98^{+3.26}_{-3.01} \times 10^{-38} L(24)^{0.877 \pm 0.015} \quad \text{for} \quad 10^{38} \lesssim L(24) \lesssim 2 \times 10^{41}, \quad (4)$$

with both luminosities in units of erg s^{-1}. The slope is indistinguishable from the one derived by D. Calzetti et al. (2010) for the luminosities of a sample of 160 ~solar metallicity, ~0.5 kpc size regions in 21 nearby galaxies, but the intercept is a factor ~1.8 higher, although the two agree within the formal uncertainties. This shift becomes obvious when comparing the luminosity surface densities (luminosity/area), as opposed to the luminosities, of the H II regions and the 0.5 kpc regions, shown in Figure 4 (right). Although the H II regions in NGC 5194 have been measured employing photometric apertures with 40% of the physical radius of the measurements in NGC 628, the derived luminosities for both cases are total H II region luminosities, implying that the photometric aperture is not the regions' characteristic size (i.e., larger or smaller apertures would not yield larger or smaller luminosities, because all luminosities are corrected for aperture losses). The choice of area is therefore somewhat arbitrary, and we choose 60 pc as the radius of the region to normalize the H II region luminosities and derive surface densities, as this is the size of the aperture radius in the more distant NGC 628 ($1\farcs4 = 63$ pc). This is the assumption used to construct the right panel of Figure 4, where we have neglected the small inclination corrections for the two galaxies. Using a different assumption for the region size, e.g., the NGC 5194 photometric aperture (~26 pc radius) causes the H II region locus to shift away from the 0.5 kpc regions by 0.05 dex, exacerbating the discrepancy between the two sets of regions. Similarly, if the H II regions in our sample are experiencing ionizing photon leakage, the discrepancy would be further magnified: the locus of the H II regions would shift away from

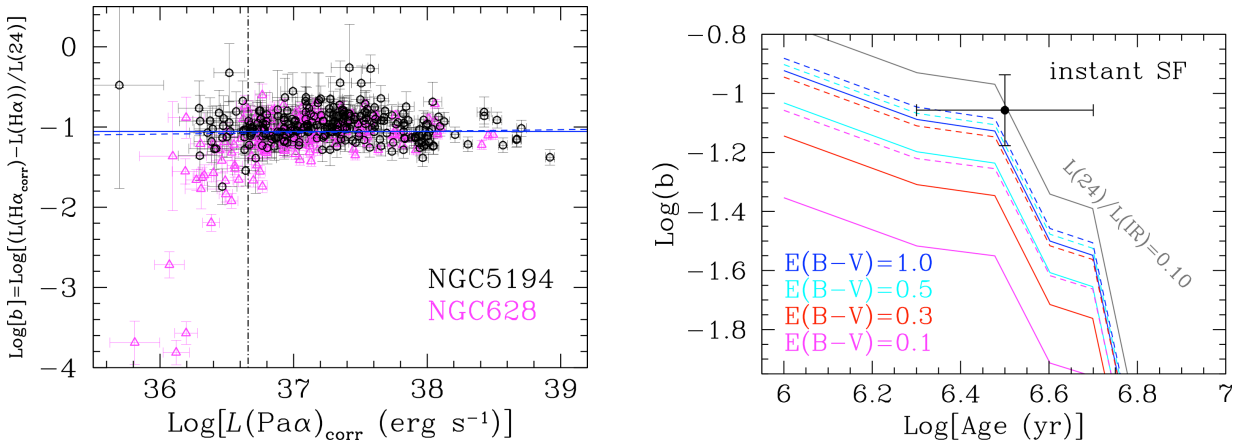

Figure 5. Left: the ratio of the nebular hydrogen emission absorbed by dust at Hα and the dust emission at 24 μm as a function of the attenuation-corrected Paα luminosity for the H II regions in NGC 5194 (black circles) and NGC 628 (magenta triangles) with 1σ uncertainties. The best linear fit, in log–log scale, and the best constant value fit for Paα luminosities above the stochastic IMF sampling limit (vertical dotted–dashed black line) are shown as dashed and continuous blue lines, respectively; the value of the scaling factor b in this regime is practically independent of the Paα luminosity. Right: the best-fit value of b from the left panel (filled circle with error bars), compared with models of instantaneous burst populations of increasing age. The observed b is assigned an age of 3 Myr with −1 Myr and +2 Myr uncertainties. Continuous [dashed] lines show models with $E(B-V)_{\rm gas} = E(B-V)$ [$E(B-V)_{\rm gas} = 2.27E(B-V)$], with different $E(B-V)$ values identified with colors (see legend). In all cases, $f = L(24)/L({\rm IR}) = 0.14$, except for the continuous gray line where $f = 0.10$ is applied to the case $E(B-V) = 0.5$ and $E(B-V)_{\rm gas} = 2.27E(B-V)$, as an example.

the 0.5 kpc region locus by ∼0.05 dex for a 50% ionizing photon loss. The best fits to the H II regions shown in Figure 4 (right panel, solid black, magenta, and blue lines) are derived using the regions that are above the stochastic IMF sampling limit in $\Sigma({\rm Pa}\alpha)_{\rm corr} = 10^{38.56}$ erg s^{-1} kpc^{-2} when normalizing to the area of a circle with a 60 pc radius. We revisit the shift between the H II region and 0.5 kpc region luminosity surface densities in Section 5, when we discuss our findings within the context of both previous results and models.

The existence of similar superlinear relations for both H II regions and larger 0.5 kpc regions lends support to the interpretation that, in both cases, the superlinear slope is mainly driven by lower-luminosity regions being more transparent to dust than more luminous regions, together with a potential increase of the mid-infrared (mid-IR) emission relative to the total IR (hotter dust) in brighter regions. In fact, neither ionizing photon leakage nor direct dust absorption of ionizing photons applies to the larger regions, as these are extended enough to include the leaked photons in their area and to encompass random collections of H II regions at a range of luminosities.

4.3. The Calibration of the Hybrid Star Formation Rate Indicators

Following several previous studies (e.g., B. Wang & T. M. Heckman 1996; V. Buat et al. 1999; G. R. Meurer et al. 1999; H. Hirashita et al. 2003; M. Treyer et al. 2010; C.-N. Hao et al. 2011; G. Liu et al. 2011; D. Calzetti et al. 2007, 2024; R. C. J. Kennicutt et al. 2007, 2009; F. Belfiore et al. 2023), we combine the IR emission with a shorter-wavelength SFR indicator, to derive a full census of the star formation energy budget in our regions. The IR probes the dust-reprocessed SFR while the short-wavelength indicator, typically UV or a nebular emission line, probes the portion of the SFR that emerges unaffected by dust. Adding the unattenuated SFR indicator should "correct" for the non-linearity of the IR SFR indicator (see previous section). Within our study, we adopt the hybrid optical–IR SFR indicator

$$\begin{aligned}{\rm SFR}(M_\odot {\rm yr}^{-1}) &= 5.45 \times 10^{-42} L({\rm H}\alpha_{\rm corr}) \\ &= 5.45 \times 10^{-42} [L({\rm H}\alpha) + bL(24)], \end{aligned} \quad (5)$$

where L(Hα) is the observed Hα luminosity and the calibration constant 5.45×10^{-42} has been derived by many authors using models (e.g., R. C. Kennicutt & N. J. Evans 2012; D. Calzetti 2013, and references therein). All luminosities are in units of erg s^{-1}. We use $L(24)$ instead of $L(21)$ for uniformity with previous derivations that leveraged the 24 μm band of Spitzer. The scaling factor b can be derived from the data directly, as shown in Figure 5 (left), where the fits to the combined data of the H II regions in NGC 5194 and NGC 628 are virtually independent of the Paα luminosity, yielding the best-fit value

$$\begin{aligned}{\rm SFR}({\rm H}\alpha + 24)(M_\odot {\rm yr}^{-1}) &= 5.45 \times 10^{-42} \\ &\times [L({\rm H}\alpha) + (0.088 \pm 0.025) L(24)], \end{aligned} \quad (6)$$

while the equivalent calibration for the 21 μm luminosity is

$$\begin{aligned}{\rm SFR}({\rm H}\alpha + 21)(M_\odot {\rm yr}^{-1}) &= 5.45 \times 10^{-42} \\ &\times [L({\rm H}\alpha) + (0.077 \pm 0.022) L(21)]. \end{aligned} \quad (7)$$

As before, the fits are performed on the 336 regions that have Paα luminosity above our adopted stochastic IMF sampling limit. The values of b derived for the combined sample are, within the uncertainties, indistinguishable from the values derived for the H II regions in NGC 628 alone, $b(24) = 0.095$ and $b(21) = 0.083$ (D. Calzetti et al. 2024). The similarities are expected, as both galaxies have solar metallicity, implying comparable amounts of dust emission per "unit" of ionizing radiation.

By definition

$$b = \frac{L({\rm H}\alpha_{\rm corr}) - L({\rm H}\alpha)}{L(24)} = \frac{L({\rm H}\alpha)_{\rm abs}}{fL({\rm bol})_{\rm abs}}, \quad (8)$$

is the Hα luminosity (ionized gas light) absorbed by dust divided by the stellar bolometric luminosity, L(bol), absorbed

by dust and emerging in the IR, and $f = L(24)/L(\mathrm{IR})$ is the fraction of IR light emerging at 24 μm. We adopt $L(\mathrm{bol})_{\mathrm{abs}} = L(\mathrm{IR})$ under the assumption of energy balance. Thus, the scaling factor b can be modeled using simplified assumptions for the SFHs and the dust distribution, since H II regions can be effectively considered instantaneous burst populations (A. Wofford et al. 2016) for which we assume foreground dust.

We generate the SEDs of instantaneous burst populations in the age range 1–10 Myr using Starburst99 models (C. Leitherer et al. 1999; G. A. Vázquez & C. Leitherer 2005) with Padova asymptotic giant branch (AGB) evolutionary tracks (L. Girardi et al. 2000), metallicity $Z = 0.02$ (solar), and a P. Kroupa (2001) IMF in the stellar mass range 0.1–120 $M_{\odot}$. The stellar models do not include pre-main-sequence stars. The stellar SEDs are attenuated by dust using a starburst attenuation curve (D. Calzetti et al. 2000) and attenuation values in the range $E(B-V) = 0.1$–1 mag. The ionized gas attenuation $E(B-V)_{\mathrm{gas}}$ is assumed to be the same as that of the stellar continuum or 2.27 times higher (D. Calzetti et al. 1994), to test the impact of both scenarios. In all cases, the attenuation of the ionized gas follows the extinction curve of K. Fahrion & G. De Marchi (2023), following the prescription of D. Calzetti et al. (1994) and D. Calzetti (2001). The fraction of IR luminosity emerging at 24 μm is assumed to be constant with age, $f = 0.14$, and we also test the effects of a smaller value, $f = 0.10$, in one case. M. Relaño et al. (2013) studied the IR SEDs of H II regions in the galaxy M33, finding that $L(24)/L(\mathrm{IR})$ spans the range $f \sim 0.07$–0.3 for the filled H II regions, which are ones from their sample most closely resembling the morphology of our H II regions. Although M33 has a lower metallicity (about 0.5 solar) than either NGC 5194 or NGC 628, the shapes of the IR SEDs of H II regions are not expected to be sensitive to these relatively small differences. We, thus, take the value $f = 0.14$ as representative of the IR SED shape of H II regions, which is also consistent with the value determined for star-forming galaxies (e.g., D. A. Dale et al. 2009; G. H. Rieke et al. 2009).

The models for b are compared with the observed value in Figure 5 (right); we assume that the observations correspond to a 3 Myr age for the H II regions (Figure 3, left), although we allow for a range in ages. The models show a general agreement with the observations for cases with significant dust ($E(B-V) \gtrsim 0.3$ mag) and with higher attenuation in the emission lines relative to the stellar continuum. Variations in the $L(24)/L(\mathrm{IR})$ ratio also have a significant impact, in the direction of favoring smaller ratios (cooler IR SEDs). Assuming ages younger than 3 Myr still maintains agreement between data and models, and accommodates some ionizing photon loss as well. For instance, a 50% leakage correction would increase b by 0.3 dex, which would still agree with the models for average cluster ages ~ 1 Myr.

4.4. H II Regions, Giant H II Regions, and Large-scale Emission

Our sample of H II regions, selected to be ionized by individual compact star clusters, leave out bright and extended emission line objects ionized by groups of closely clustered compact sources. These objects would have appeared only partially resolved in past ground-based imaging, and, because of their brightness and extent, were termed giant H II regions (e.g., M. G. Smith & D. W. Weedman 1970; R. Terlevich & J. Melnick 1981; J. S. Gallagher & D. A. Hunter 1983; J. M. van der Hulst et al. 1988). We identify 13 giant H II regions within the 4.4×12.6 kpc^2 JWST mosaic footprint (Figure 6): nine of those regions include 15 of the single-source H II regions from our sample and the remaining four have no sources that can be easily isolated from the rest of the region. As the giant H II regions provide significant contribution to the line emission encompassed by the mosaics, we measure their luminosities and check whether their inclusion would change any of the results from the previous sections. We also calculate the fraction of the total emission within the JWST footprint captured by the single-source and giant H II regions, both in line emission and in the mid-IR.

The giant H II regions require customized apertures for the photometry, as their sizes vary depending on the number and mix of ages and masses of the clusters that ionize them. We select aperture sizes to include the 21 μm emission out to within 3σ of the local background, resulting in radii between $2''$ and $5''.5$ (73–200 pc), depending on the region (Table 4). The same quantities that were measured for the H II regions are measured for the giant H II regions, including luminosities, EWs, etc. Aperture corrections are not required for Hα and Paα, but small aperture-dependent corrections are applied to the 21 μm luminosities. Table 4 lists for each of the 13 giant H II Regions the ID, location on the sky in R.A.(2000) and decl.(2000), the radius of the aperture used for photometry, the observed luminosity in Hα, Paα, and 21 μm, the EW in Paα, and the color excess $E(B-V)$. Both Hα and Paα are reported already corrected for Milky Way foreground extinction.

As expected, the giant H II regions have larger luminosities, on average, than the H II regions, but also span a more restricted range of values both in EW(Paα) and $E(B-V)$ (Figure 7, top two panels). The values of EW(Paα), which are lower than those of the H II regions at a given Paα luminosity, can be explained with a contribution to the stellar continuum both by multiple clusters with different ages and by the larger apertures employed to measure the giant H II regions, which admit a larger fraction of background stellar emission (see discussion in Section 4.1). Differential dust attenuation between nebular emission and stellar continuum, which is likely to occur when considering large spatial scales and stellar population mix, can also contribute to decreasing the EW(Paα) values; for the observed range of $E(B-V)$ the expected decrease can be as much as 0.08–0.18 dex. If the EWs are interpreted strictly in terms of mean ages, the giant H II regions are in the age range of 3.5–5.5 Myr, only marginally older than the single-source H II regions.

The color excess of the giant H II regions is within the range spanned by the H II regions (Figure 7, top-right panel), when using luminosity surface densities instead of luminosities, to account for the differences in area used to measure the giant H II and single-source H II regions. The models from D. Calzetti et al. (2007) are shown as blue lines (Equation (B2)).

The giant H II region luminosities fill in the bright luminosity end of the distribution of the H II regions (Figure 7, bottom left), marking the same trend for $L(21)$ versus $L(\mathrm{Pa}\alpha)_{\mathrm{corr}}$. A formal fit through the H II regions of NGC 5194 and NGC 628, including the giant H II regions discussed in this section, yields a slope of 1.12 ± 0.02, consistent within 1σ with the slope reported in Equation (2). Not surprisingly, the giant H II regions distribute around the

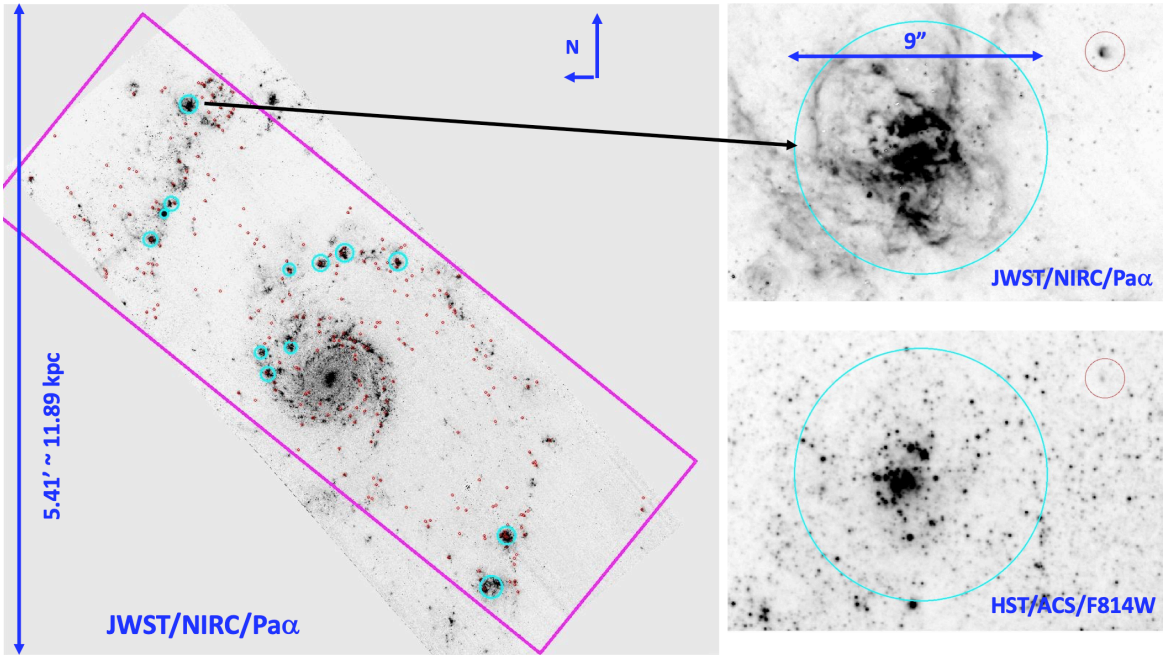

Figure 6. Left: the JWST Paα mosaic with the 13 giant H II regions (cyan circles) together with the 254 H II regions (red circles). The radii of the circles match those of the apertures used for photometry, which for the giant H II regions range from 2″ and 5.″5. North is up and east is left. The magenta rectangle shows the MIRI 21 μm footprint. Right, top, and bottom: detailed views showing one giant H II region (cyan circle, its location marked by the black arrow) and one H II region (red circle) in the JWST/Paα image (top right) and the HST/ACS F814W image (bottom right). The diameter of the cyan circle, 9″, is indicated for reference. The Paα image highlights the complexity of the ionized gas emission from the giant H II region, while the F814W image shows the multiplicity of the continuum sources ionizing the gas; conversely, the H II region (red circle) is dominated by a single, compact source.

Table 4
Source Locations, Luminosities, and Derived Quantities for the Giant H II Regions in NGC 5194

ID (1)	R.A.(2000), Decl.(2000) (2)	Radius (3)	Log[L(Hα)] (4)	Log[L(Paα)] (5)	Log[L(21)] (6)	Log[EW(Paα)] (7)	$E(B-V)$ (8)
G1	13:29:55.7640,+47:11:44.489	3.5	38.873 ± 0.028	38.724 ± 0.018	41.053 ± 0.052	2.816 ± 0.027	1.005 ± 0.045
G2	13:29:54.6436,+47:11:57.720	3.0	38.402 ± 0.034	38.153 ± 0.024	40.323 ± 0.064	2.353 ± 0.032	0.870 ± 0.056
G3	13:29:54.6943,+47:12:36.450	3.0	38.494 ± 0.032	38.237 ± 0.023	40.361 ± 0.063	2.462 ± 0.031	0.859 ± 0.054
G4	13:29:53.1800,+47:12:39.760	4.0	39.007 ± 0.027	38.587 ± 0.019	40.597 ± 0.063	2.743 ± 0.028	0.638 ± 0.045
G5	13:29:52.0107,+47:12:44.770	4.5	39.241 ± 0.025	38.806 ± 0.018	41.002 ± 0.056	2.747 ± 0.025	0.618 ± 0.041
G6	13:29:49.3892,+47:12:40.510	4.5	38.899 ± 0.028	38.734 ± 0.018	40.980 ± 0.057	2.836 ± 0.027	0.983 ± 0.045
G7	13:29:44.0821,+47:10:23.813	4.5	39.508 ± 0.024	39.076 ± 0.016	41.145 ± 0.054	2.971 ± 0.024	0.623 ± 0.039
G8	13:29:44.8174,+47:09:58.070	5.5	39.318 ± 0.025	38.911 ± 0.017	40.982 ± 0.060	2.581 ± 0.023	0.657 ± 0.041
G9	13:29:59.6235,+47:13:59.019	4.5	39.365 ± 0.025	38.824 ± 0.017	40.653 ± 0.064	2.807 ± 0.025	0.475 ± 0.041
G10	13:30:01.4968,+47:12:51.728	3.5	38.894 ± 0.028	38.782 ± 0.018	41.305 ± 0.049	2.744 ± 0.025	1.055 ± 0.045
G11	13:30:00.4693,+47:13:09.574	3.5	38.876 ± 0.028	38.424 ± 0.021	40.506 ± 0.063	2.662 ± 0.030	0.596 ± 0.047
G12	13:29:56.1027,+47:11:55.183	3.0	38.640 ± 0.031	38.255 ± 0.023	40.207 ± 0.068	2.322 ± 0.030	0.686 ± 0.051
G13	13:30:00.8440,+47:13:04.439	2.0	38.706 ± 0.030	38.355 ± 0.021	40.301 ± 0.057	2.924 ± 0.034	0.732 ± 0.049

Notes. (1) The identification number of the source. (2) R.A. and decl. in J2000 coordinates. (3) Radius, in arcseconds, of the photometric aperture used for photometry. (4)–(6) Logarithm of the luminosity of each source at the indicated wavelength, in units of erg s^{-1}. The Hα and Paα luminosities are corrected for Milky Way foreground extinction. (7) The logarithm of the EW of Paα, in Å units, calculated from the ratio of the emission line flux to the stellar continuum flux density. (8) The color excess, $E(B-V)$, in magnitudes, derived from the Hα/Paα luminosity ratio.

same value of the scaling factor b as the H II regions (Figure 7, bottom right). In summary, the giant H II regions are consistent with being brighter versions of the single-source H II regions but similarly young, likely because their luminosity is dominated by the youngest members in the groups of clusters that ionize them.

The photometry of the giant H II regions is measured in regions with sizes almost as large as those used by D. Calzetti et al. (2007) for their measurements of this galaxy. The photometric sizes (6.″5 radii) used in that paper were driven by the low resolution of the Spitzer/MIPS 24 μm channel (G. H. Rieke et al. 2004), while our large apertures (Table 4) are driven by the extent of the 21 μm and Paα emission. We thus discuss the level of overlap between our sample and the sample from D. Calzetti et al. (2007). Of the 39 regions in common between our footprint and the footprint of the 24 μm, Paα, and Hα observations used in D. Calzetti et al. (2007), only seven are among our giant H II regions. The remaining

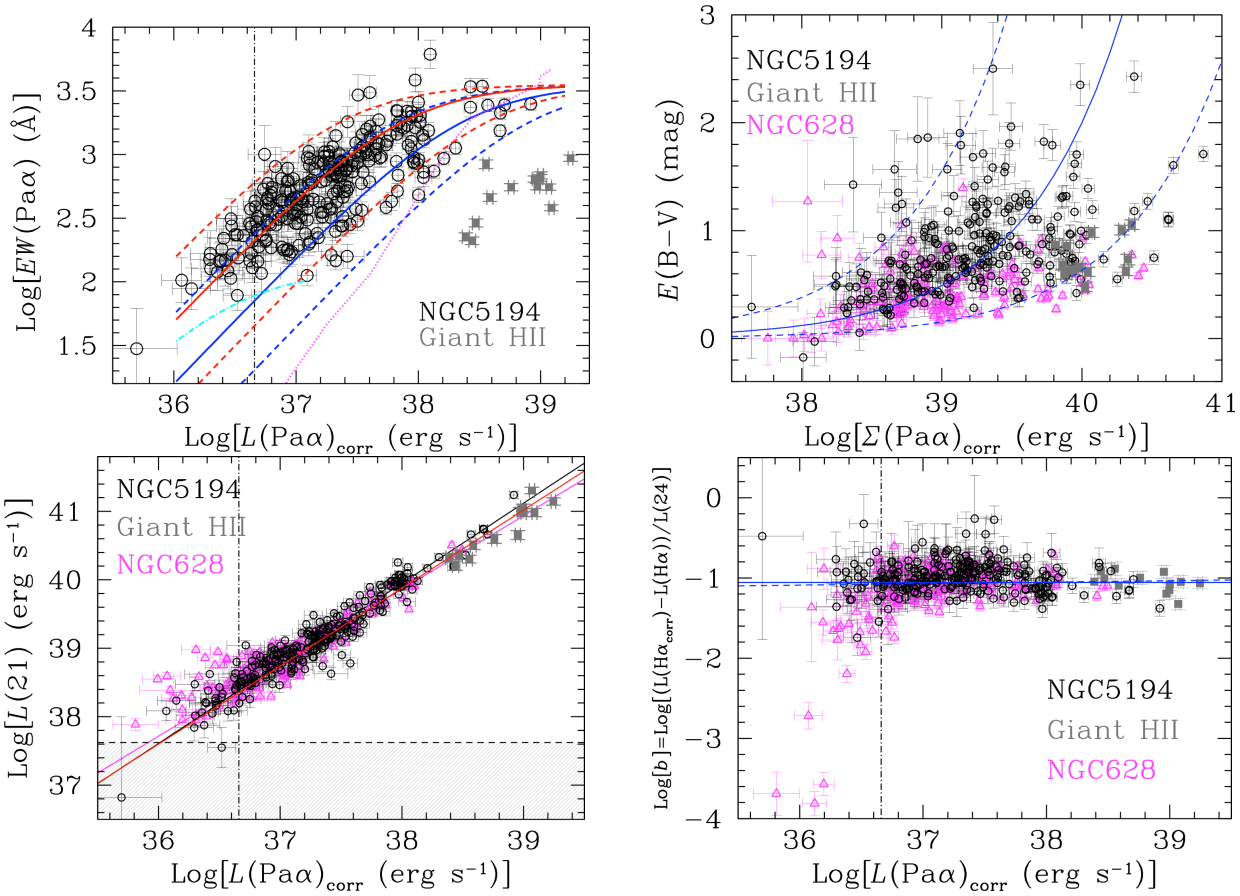

Figure 7. The same plots as the left and right panels of Figure 3 (top left and top right, respectively), the left panel of Figure 4 (bottom left), and the left panel of Figure 5 (bottom right), with the giant H II regions in NGC 5194 added as gray filled squares. In the top-right panel, the luminosity surface density $\Sigma(\mathrm{Pa}\alpha)_{\mathrm{corr}}$ is used instead of the luminosity $L(\mathrm{Pa}\alpha)_{\mathrm{corr}}$.

sources are broken down each into multiple single-source H II regions in our analysis. Thus, the 0.5 kpc regions identified by D. Calzetti et al. (2007) as peaks of 24 μm emission contain a mix of sources, including giant H II regions and individual H II regions with a variety of spatial distributions. Because of these differences, in the remainder of this paper we will treat the giant H II regions as more luminous versions of H II regions, while the regions from D. Calzetti et al. (2007) will be treated as general representatives of star formation over ∼0.5 kpc scales in galaxies.

We compare the summed total Hα, Paα, and 21 μm luminosities from the H II regions and giant H II regions with the luminosity captured by the entire JWST footprint, to evaluate whether our sample is representative of the full H II region population. Table 5 lists the observed and attenuation-corrected luminosities for the JWST footprint, for the sum of the H II regions above the stochastic IMF sampling limit of $\mathrm{Log}[L(\mathrm{Pa}\alpha)_{\mathrm{corr}}] = 36.66$ (after removing the 15 regions which are contained within the giant H II regions) and for the sum of the giant H II regions. Table 5 also reports the luminosity-weighted $E(B-V)$ values for all three cases, showing that the JWST footprint suffers from, as expected, lower dust attenuation than the H II regions, and the giant H II regions are slightly less attenuated than the single-source H II regions. For reference, the single-source H II regions have a median $E(B-V) \sim 0.8$ mag and the giant H II regions have $E(B-V) \sim 0.7$ mag, similar to the luminosity-weighted values in Table 5.

As discussed earlier, the minimum luminosity for the H II regions to be considered above the stochastic IMF sampling limit corresponds to a star cluster with mass = 3000 $M_{\odot}$ and age = 4 Myr. Roughly equal masses are in star clusters above and below 3000 $M_{\odot}$ (A. Adamo et al. 2020), implying that the H II regions include about twice as much luminosity as the ones reported in Table 5. We add the faint H II region luminosities under two assumptions: that their dust attenuation is similar to the one of the H II regions above the stochastic IMF sampling limit (A. Knutas et al. 2025) and that their attenuation is the same as the mean attenuation of the JWST footprint (Table 5). These two assumptions yield slightly different values of the attenuation-corrected Hα and Paα luminosities for the JWST footprint, as listed in Table 5 (lines 2 and 3). The contribution of the giant H II regions is added to the H II regions without extrapolations in their total luminosity, under the reasonable assumptions that the giant H II regions include clusters that sample the full range of masses within the age range of interest (∼0–6 Myr).

Taking those calculations at face value, the Hα luminosity of all H II regions (normal and giant) represents 43%–47% of the total within the JWST footprint, depending on the assumption for the attenuation of the faint H II regions. For Paα, the fraction is about 51%–54%. For both, we find that the H II regions represent about half of the recovered ionizing photons, with the remaining half found in the diffused ionized medium, as typical of star-forming disks (M. S. Oey et al. 2007). The difference between the Hα and Paα diffuse

Table 5
Total Luminosities in NGC 5194

Source (1)	(2)	Log[L(Hα)] (3)	Log[L(Paα)] (4)	Log[L(21)] (5)	$E(B-V)$ (6)
JWST Footprint[a]	Observed	41.21	40.52	42.95	0.27
	Corrected	41.64	40.67	⋯	⋯
	⋯	41.60	40.65	⋯	⋯
H II Regions (>stochastic limit)[b]	Observed	39.836 ± 0.005	39.560 ± 0.004	41.744 ± 0.006	0.833 ± 0.009
	Corrected	40.729 ± 0.005	39.836 ± 0.013	⋯	⋯
Giant H II Regions [c]	Observed	40.174 ± 0.009	39.804 ± 0.004	41.974 ± 0.019	0.71 ± 0.01
	Corrected	40.898 ± 0.007	40.005 ± 0.016	⋯	⋯

Notes. (1) The region's or the sum of the regions' luminosities. (2) For each source, the first line indicates the observed luminosities and the second line is for the attenuation-corrected luminosities. For the JWST footprint, the second and third lines are for two separate assumptions on the attenuation of the faint H II regions: the second line assumes the faint regions have the same dust attenuation as the bright ones (>stochastic limit) and the third line assumes the faint regions have the same attenuation as the diffuse emission (see text for details). (3)–(5) Logarithm of the luminosity of each source at the indicated wavelength, in units of erg s^{-1}. The Hα and Paα luminosities are corrected for Milky Way foreground extinction. (6) Luminosity-weighted color excess, in magnitudes.
[a] Luminosities for the JWST footprints are given without uncertainties. The formal uncertainties are small, but systematics are difficult to control.
[b] Sum of the luminosities of the H II regions (after removal of the regions contained within the giant H II regions) that are above the stochastic IMF sampling limit of $\mathrm{Log}[L(\mathrm{Pa}\alpha)_{\mathrm{corr}}] = 36.66$.
[c] Sum of the luminosities of the giant H II regions.

fractions, ∼55% and ∼47%, respectively, is negligible within the uncertainties of our estimate, but, if confirmed, would support models where a small fraction, ∼20%, of the Hα diffuse light is due to reflection by dust (R. Dong & B. T. Draine 2011; L. McCallum et al. 2025); the Paα line would then be expected to have a smaller reflection component, since the wavelength of Paα has a lower scattering cross section, by a factor of several, than Hα (J. C. Weingartner & B. T. Draine 2001). We refrain from speculating further on the nature of this difference as we do not control some of the systematics, such as small uncertainties in the stellar background removal, the small gradient in the Paα mosaic (corresponding to 1σ change from top to bottom), and faint residual $1/f$ noise in the NIRCam images.[44] From the result of this analysis, we conclude that our sample is representative of the H II region population within the JWST footprint in NGC 5194.

We have a better handle on the potential systematics for the 21 μm luminosity within the JWST footprint thanks to the Spitzer/MIPS 24 μm image of the galaxy. Matching the JWST footprint to the MIPS image yields a flux density of 8.17 Jy at 24 μm, to be compared with 8.91 Jy at 21 μm, or 9% lower, which can be ascribed to small uncertainties in matching the two mosaics. Thus, we conclude that the JWST mosaic includes the diffuse emission from the galaxy. When comparing the emission from the full population of H II regions (giant and normal) to the total, we find that the regions account for 23% of the 21 μm emission in the JWST footprint, or about half of the fraction in the ionized gas. The nature of this difference is discussed in the next section.

5. Discussion

5.1. Modeling the Age Dependence of the Hybrid Infrared Star Formation Rate Calibrations

The value of b at 24 μm (Equation (8) and Figure 5) derived for the H II regions in the two galaxies NGC 5194 and NGC 628 can be compared with derivations of the same scaling factor by other authors. Here we expand on the discussion presented in D. Calzetti et al. (2024) by adding stellar population models that take into account different possible SFHs when comparing the scaling factor b between regions of different sizes, including whole galaxies. Table 6 summarizes previous results for ease of comparison. The H II region results of F. Belfiore et al. (2023) are considered lower limits in this work, as those authors' fits include regions affected by stochastic IMF sampling, which lower the best-fit b value (M. Fumagalli et al. 2011). Despite the limited number of available measurements, it is clear, as already remarked in D. Calzetti et al. (2024), that b decreases in value for increasing region sizes; in particular b is ∼4.4 times larger in H II regions than in whole galaxies.

To test how well these scaling factors work, we combine our sample of H II regions with the sample of ∼0.5 kpc regions discussed in Section 4.2 and other samples of kiloparsec-sized regions and whole galaxies for which L(Pα), L(Hα), and L(24) are available, using data from the literature. We add the 21 ∼2 kpc regions analyzed by D. Calzetti et al. (2007), integrated measures for 46 local star-forming galaxies from the SINGS sample (R. C. J. Kennicutt et al. 2009), 10 local starburst galaxies from C. W. Engelbracht et al. (2008), and a sample of 24 luminous IR galaxies from A. Alonso-Herrero et al. (2006). For the luminous IR galaxy samples, only IRAS 25 μm data are available; R. C. J. Kennicutt et al. (2009) showed that these are indistinguishable from the Spitzer 24 μm measurements. In addition, the luminous IR galaxies lack Hα measurements and we make the reasonable assumption that L(Hα) is negligible relative to L(24). The Paα emission for the starbursts from the sample of C. W. Engelbracht et al. (2008) is not corrected for dust attenuation due to the aperture mismatch between the Hα data, which are the the whole galaxy, and the Paα data, which are for the inner 50″ diameter region. Thus, the Paα luminosity for this sample is underestimated, possibly by up to 65%, depending on the amount of attenuation present in the galaxies. For the Hα luminosity of the starbursts, from C. W. Engelbracht et al. (2008) updated using the survey by R. C. J. Kennicutt et al. (2008) where possible, we only use the observed values

[44] https://jwst-docs.stsci.edu/known-issues-with-jwst-data/1-f-noise#gsc.tab=0

Table 6
Infrared Scaling Factor for the Hybrid Star Formation Rate

Region Diameter	τ[a] (Myr)	b[b]	References
50–120 pc	2–5	0.088 ± 0.025	This work, D. Calzetti et al. (2024)
∼100 pc	2–5	>0.035	F. Belfiore et al. (2023)[c]
∼500 pc	40–60	0.038 ± 0.005	R. C. J. Kennicutt et al. (2007)[d]
∼500 pc	30–130	0.031 ± 0.006	D. Calzetti et al. (2007)[e]
>10 kpc	∼10,000	0.022 ± 0.002	Y.-N. Zhu et al. (2008)[f]
>10 kpc	∼10,000	0.020 ± 0.005	R. C. J. Kennicutt et al. (2009)[g]

Notes.
[a] Star formation duration attributed to the region, see text.
[b] Best-fit $L(24)/L(\mathrm{H}\alpha)$ scaling constant for the hybrid $\mathrm{H}\alpha + 24$ SFR indicator.
[c] Derived from ∼20,000 H II regions in 19 galaxies, including regions affected by stochastic IMF sampling. The scaling parameter increases to $b \sim 0.08$–0.09, when excluding such regions in the F. Belfiore et al. (2023) sample.
[d] Derived from 42 regions in NGC 5194.
[e] Derived from 160 regions in 21 ∼solar metallicity galaxies.
[f] Derived from 379 galaxies star-forming galaxies.
[g] Derived from 68 nearby (<140 Mpc) star-forming galaxies.

in what follows. For the SINGS sample of galaxies, only $\mathrm{H}\alpha$, attenuation-corrected using $\mathrm{H}\beta$ (0.4861 μm), is available; we assume that, in star-forming galaxies, the ionized gas luminosity is dominated by emission from low-extinction regions, and the $\mathrm{H}\alpha/\mathrm{H}\beta$ ratio is sufficient to recover the intrinsic luminosity (R. C. J. Kennicutt et al. 2009; R. C. Kennicutt & N. J. Evans 2012). The attenuation-corrected $\mathrm{H}\alpha$ is converted to an equivalent $\mathrm{Pa}\alpha$ by assuming $\mathrm{H}\alpha/\mathrm{Pa}\alpha = 7.82$. The samples from D. Calzetti et al. (2007) and R. C. J. Kennicutt et al. (2009) are not independent: they are all drawn from the SINGS sample, although the two papers analyze different region sizes. In total, the combined sample of H II regions, galactic regions, and galaxies has 658 data points.

The data from the different samples are shown in Figure 8, left, using the scaling factor value appropriate for each sample: $b = 0.088$ for the H II region samples of NGC 628 and NGC 5194; $b = 0.031$ for the ∼kiloparsec-sized regions from D. Calzetti et al. (2007); and $b = 0.020$ for the galaxy samples of R. C. J. Kennicutt et al. (2009), C. W. Engelbracht et al. (2008), and A. Alonso-Herrero et al. (2006). The one-to-one line (in log–log luminosity scale) is shown on the plot for comparison. The histogram of the distribution of the data relative to the one-to-one line for the three subsamples—H II regions, galaxy regions, and whole galaxies—is shown in Figure 8, right. The data points are reasonably well distributed around the one-to-one line, when using the b value appropriate for each subsample. The source showing the most deviation from this trend in Figure 8, left, is from the sample of A. Alonso-Herrero et al. (2006). As noted by these authors, the galaxy, IC 860, may include an active galactic nucleus, which would explain its overluminous 24 μm emission relative to $\mathrm{Pa}\alpha$.

The models of the scaling factor are developed in Appendix A, using the definition in Equation (8) to derive b from the SEDs of stellar populations; here we outline the basic approach. The $\mathrm{H}\alpha$ emission is almost entirely contributed by photoionization in galaxies, with only a small contribution from other processes (e.g., shocks; R. J. Reynolds 1984, 1990; A. M. N. Ferguson et al. 1996; C. G. Hoopes et al. 1996; C. G. Hoopes & R. A. M. Walterbos 2003; E. S. Voges & R. A. M. Walterbos 2006; M. S. Oey et al. 2007; K. Zhang et al. 2017). This implies that populations younger than 6 Myr are required for modeling $L(\mathrm{H}\alpha)_{\mathrm{abs}}$ in Equation (8). When modeling galaxies or large (≫100 pc) regions, star formation can be considered constant over these timescales.

Conversely, the IR emission is contributed by stellar populations of all ages, including gigayear-old ones (C. J. Lonsdale Persson & G. Helou 1987; V. Buat & J. M. Deharveng 1988; M. Rowan-Robinson & J. Crawford 1989; M. Sauvage & T. X. Thuan 1992; V. Buat & C. Xu 1996; R. A. M. Walterbos & B. Greenawalt 1996; D. Calzetti et al. 2010; G. J. Bendo et al. 2012; D. A. Dale et al. 2012; D. J. B. Smith et al. 2012; B. Magnelli et al. 2014; M. Boquien et al. 2016; B. Gregg et al. 2022; A. K. Leroy et al. 2023). Modeling $L(24) = fL(\mathrm{bol})_{\mathrm{abs}}$ (Equation (8)) requires analyzing the possible ranges of f and $L(\mathrm{bol})_{\mathrm{abs}}$, separately. The fraction of IR emission emerging at 24 μm, f, changes by less than a factor of 3 in galaxies and 4 in H II regions (G. H. Rieke et al. 2009; D. Calzetti et al. 2010; M. Relaño et al. 2013); however, this change is linked to surface brightness, not region size, and the surface brightness of H II regions has significant overlap with the surface brightness of large galaxy regions (e.g., Figure 4, right). We use $f = 0.14$ as a reference value for the models, which is a mean value for both H II regions and star-forming galaxies, although variations to this assumption are also explored.

$L(\mathrm{bol})_{\mathrm{abs}}$ increases with increasing $E(B-V)$ and/or increasing bolometric output of the stellar population. At constant SFR, the latter can only occur by increasing the duration τ of the star formation, which progressively increases the population of low-mass, long-lived stars and the light they contribute to the nonionizing SED. A simple increase in $E(B-V)$ cannot explain the decrease of b with increasing region size, since, as shown in Table 5, galaxies and large regions of galaxies are less extincted on average than the H II regions they contain. This has already been reported in the literature and is also seen in Figure 3, right, where the extinction–luminosity relation for galaxies by T. Garn & P. N. Best (2010) marks the lower envelope of the same relation for H II regions. Appendix A presents the expected trend of the b scaling factor as a function of the star formation duration τ, for different assumptions of the SFH (constant, exponentially decreasing, and exponentially increasing), of the

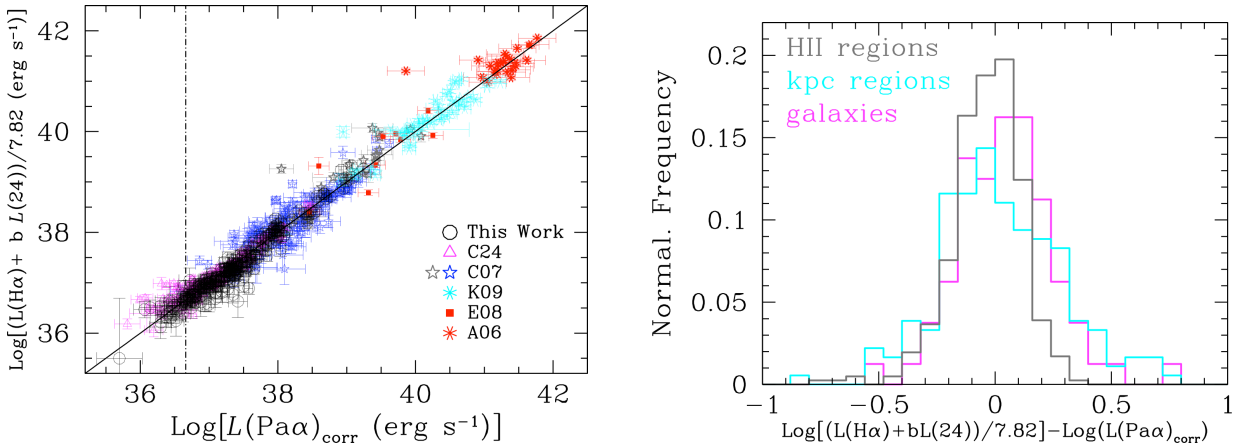

Figure 8. Left: the hybrid $[L(\mathrm{H}\alpha) + bL(24)]$ luminosity as a function of the attenuation-corrected Paα luminosity for several samples: the H II regions in NGC 5194 (black empty circles, this work) and in NGC 628 (magenta empty triangles, D. Calzetti et al. 2024, denoted C24); the 0.5 kpc regions (blue stars) and 2 kpc (gray stars) regions from D. Calzetti et al. (2007, denoted C07); the integrated galaxy measurements of star-forming galaxies by R. C. J. Kennicutt et al. (2009, cyan asterisks, denoted K09), of local starburst galaxies by C. W. Engelbracht et al. (2008, red filled squares, denoted E08), and of luminous IR galaxies by A. Alonso-Herrero et al. (2006, red asterisks, denoted A06). All data are shown with 1σ uncertainties. The hybrid luminosity is divided by 7.82 (the Hα/Paα ratio) to bring the two axes to the same luminosity range. For each subsample, H II regions, kiloparsec-size regions, and whole galaxies, the appropriate value of the scaling factor b is adopted: 0.088, 0.031, and 0.020, respectively. The one-to-one relation is shown as a black solid line. The transition luminosity above which stochastic sampling of the IMF is mitigated is shown as a vertical dotted–dashed line. Right: the histogram of the data in the left panel relative to the one-to-one line, divided according to subsample: H II regions (gray histogram, samples from this work and D. Calzetti et al. 2024), kiloparsec-size regions (cyan histogram, samples from D. Calzetti et al. 2007), and whole galaxies (magenta histogram, samples from R. C. J. Kennicutt et al. 2009; C. W. Engelbracht et al. 2008; A. Alonso-Herrero et al. 2006).

amount of dust attenuation in populations of different ages, and of the amount of dust attenuation in the ionized gas.

In order to compare the models with the observed b values, we need to relate star formation duration to region size. We leverage the fact that (1) our measurements are obtained in regions where the background emission from the galaxy has been removed, and (2) star formation is hierarchically clustered out to about 1 kpc or so and larger scales correspond to older mean ages for the stellar populations (e.g., Y. N. Efremov & B. G. Elmegreen 1998; R. de la Fuente Marcos & C. de la Fuente Marcos 2009; B. G. Elmegreen 2011; K. Grasha et al. 2015; D. A. Gouliermis et al. 2015; K. Grasha et al. 2017a, 2017b; B. G. Elmegreen 2018; D. A. Gouliermis 2018; G. Shashank et al. 2025). Because of (1), the subgalactic regions can be attributed the mean ages that are appropriate for their location in the hierarchy.

For the H II regions, we adopt the mean age we derive from the EW versus luminosity trend (Figure 3, left), $\tau \sim 3$ Myr, with some uncertainty attached to this value to span the range of possible H II region ages (see Table 6). For this discussion, we equate the mean b value of the H II regions to the expected b value resulting from constant star formation over $\tau \sim$ a few megayears. While this equivalence is generally not true, we argue that it is reasonable in our case for the following reason. Our sample of >300 H II regions is likely to distribute uniformly in age over the range ~0–6 Myr (Section 4.1) and we select our regions to be massive enough to be above the limit of stochastic sampling for the stellar IMF, limiting the effects of biases in deriving the average Hα and IR luminosities. Thus, this large sample is equivalent to sampling an event of constant star formation over the timescale range listed in Table 6.

For the ~kiloparsec regions, we use the crossing times of stars and star clusters. Cluster-to-cluster dispersion velocities range from a few kilometers per second to ~20 km s^{-1} out to ~1 kpc (B. C. Whitmore et al. 2005; K. Grasha et al. 2017b). Gas dispersion velocities due to turbulence are relatively small, ~1–2 km s^{-1} (M. H. Heyer & C. M. Brunt 2004; M. Heyer et al. 2009), and the same small values are likely inherited by the stars; however, shear could increase the velocities by a factor of a few and shear rather than turbulence may be at the root of the observed hierarchy of star formation (B. G. Elmegreen 2018). With these velocities, we obtain a crossing time of 30–130 Myr for 0.5 kpc. This timescale agrees with the one measured from the age–separation relation of star clusters in several galaxies, which supports the turbulent star formation scenario (Y. N. Efremov & B. G. Elmegreen 1998; R. de la Fuente Marcos & C. de la Fuente Marcos 2009; K. Grasha et al. 2017b). For the specific case of NGC 5194, K. Grasha et al. (2017b) derive a timescale of about 40–60 Myr at 0.5 kpc. As a caveat, these adopted timescales are subject to additional uncertainty, as crossing times are inversely proportional to the quarter power of pressure (B. G. Elmegreen 1989) and interstellar medium pressure can change by over an order of magnitude within star-forming galaxies (M. Querejeta et al. 2023), and more in starbursts and mergers. For whole galaxies, we assume that the duration of the star formation is $\gtrsim$10 Gyr.

The models from Appendix A are used here for comparison with the observed b (Figure 9, left). The models are a good representation of the trend of the scaling factor b with τ, although we need to keep in mind that there is nonnegligible scatter in the models for different parameter choices, including, but not limited to, dust attenuation in both the stellar populations and the ionized gas, the fraction of IR emission emerging at 24 μm, and, to a lesser extent, the SFH. We provide an analytical expression for b as a function of star formation duration τ, by interpolating through the observational data, including their scatter:

$$\mathrm{SFR}(M_\odot \mathrm{yr}^{-1}) = 5.45 \times 10^{-42}[L(\mathrm{H}\alpha) + b(\tau)L(24)], \quad (9)$$

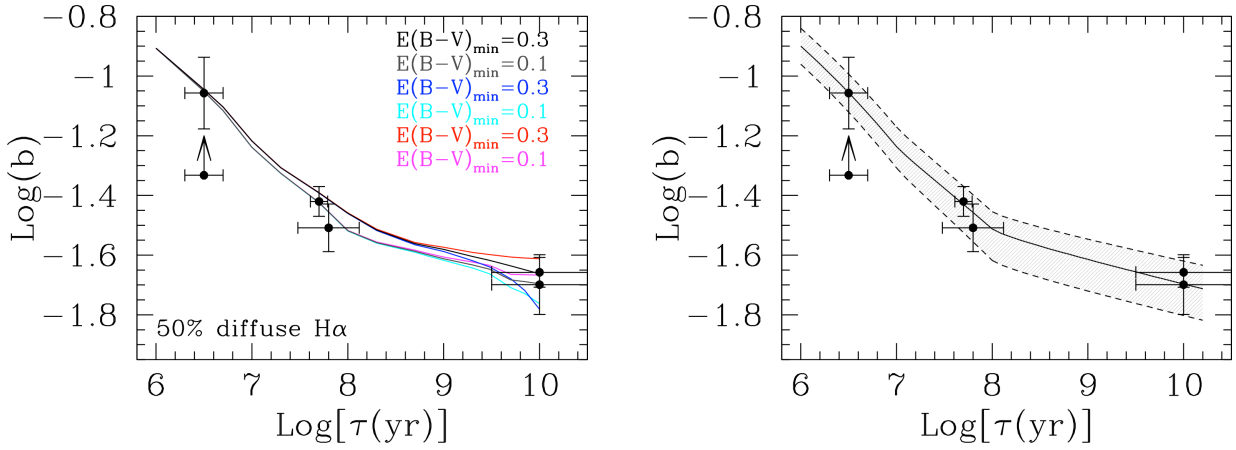

Figure 9. Left: the scaling factor b as a function of the duration of star formation τ for the data listed in Table 6, compared with model expectations. Three SFHs are included, with decreasing color excess for stellar populations of increasing age and 50% clustered–50% diffuse Hα emission, as described in Appendix A. $f = 0.14$ for this model. The three SFHs are constant (black and gray lines), decreasing (blue and cyan lines), and increasing (red and magenta) star formation with τ, see details in Appendix A. Right: the smooth analytical representation of the trend of the scaling factor b and its scatter as a function of star formation duration, as described in Equation (10), shown as black continuous and dashed lines, respectively.

where $b(\tau)$ can be written as

$$\begin{aligned}\mathrm{Log}[b(\tau)] &= 0.1^{+0.06}_{-0.06} - \exp\left[\frac{(\mathrm{Log}(\tau) - 6.)}{3.45^{+0.05}_{-0.10}}\right] \\ &\quad \text{for} \quad 6.\leqslant \mathrm{Log}(\tau) < 7., \\ &= -0.236^{+0.065}_{-0.072} - \exp\left[\frac{(\mathrm{Log}(\tau) - 7.)^{0.9}}{4.10^{-0.10}_{-0.40}}\right] \\ &\quad \text{for} \quad 7.\leqslant \mathrm{Log}(\tau) < 8., \\ &= -0.512^{+0.058}_{-0.106} - \exp\left[\frac{(\mathrm{Log}(\tau) - 8.)^{0.8}}{10.3^{+1.1}_{-0.0}}\right] \\ &\quad \text{for} \quad 8.\leqslant \mathrm{Log}(\tau) \leqslant 10., \end{aligned} \tag{10}$$

where the timescale τ is in years, and $b(\tau)$ is nondimensional. Figure 9, right, shows the above analytic expression in relation to the observations. The superscript (subscript) for each coefficient in Equation (10) marks the upper (lower) envelope in the figure.

For all practical purposes, Equations (9) and (10) can be used to derive SFRs for systems with star formation durations between ∼1 Myr and ∼10 Gyr, with an accuracy that depends on the relative luminosity of the Hα to the 24 μm emission, but is about 25%–30% at all ages.

The above calibration has been derived for ∼solar metallicity systems and metallicity is expected to have second-order effects on $b(\tau)$. The absorbed portion of *both* L(Hα) and L(bol) decreases for decreasing dust content, and, therefore, decreasing metallicity, with a similar dependence on $E(B-V)$ (D. Calzetti et al. 2024). This implies that, to first order, the ratio $L(\mathrm{H}\alpha)/L(\mathrm{bol})$ does not change with $E(B-V)$. However, the ionizing photon rate is dependent on metallicity, being higher at lower metal content (J. Chisholm et al. 2019), which affects the nebular line luminosities, and can result in an increase of $b(\tau)$ for decreasing metallicity. Finally, $f = L(24)/L$(IR) can also depend on metallicity (e.g., A. Rémy-Ruyer et al. 2015).

5.2. Calibration of the 24 μm Star Formation Rate from H II Regions to Galaxies

In Section 4.2 we briefly presented four mechanisms which may be the source of the superlinear correlation (in log–log scale) between $L(24)$ (or $L(21)$) and $L(\mathrm{Pa}\alpha)_{\mathrm{corr}}$, and which we summarize here again for clarity:

1. lower-luminosity regions/galaxies tend to be less extincted than brighter ones, implying that a larger fraction of the ionizing and nonionizing photons at low luminosities emerges directly in the UV and optical and are not captured by the IR emission; this depresses $L(24)$ relative to $L(\mathrm{Pa}\alpha)_{\mathrm{corr}}$ for fainter regions relative to brighter ones;
2. leakage of ionizing photons out of H II regions affects bright regions more than faint ones (E. W. Pellegrini et al. 2012), depressing $L(\mathrm{Pa}\alpha)_{\mathrm{corr}}$ at high luminosity more than at low luminosity, while leaving $L(24)$ unaffected;
3. direct absorption of ionizing photons by dust, which depresses the $L(\mathrm{Pa}\alpha)_{\mathrm{corr}}$ of bright (dustier) regions proportionally more than fainter (less dusty) regions and which may accompany the first mechanism for sufficiently high dust content (A. K. Inoue et al. 2001; M. A. Dopita et al. 2003; M. R. Krumholz & C. D. Matzner 2009; B. T. Draine 2011); and
4. higher-luminosity regions produce "hotter" IR SEDs, which increase the fraction of 24 μm emission relative to the total IR emission (M. Relaño et al. 2013; G. H. Rieke et al. 2009; D. Calzetti et al. 2010). Although we do not discuss the exact nature of "hotter" IR SEDs, we note that dust temperature may not be the only cause of enhanced $L(24)/L$(IR) values; M. Relaño et al. (2018), for instance, find that shattering of large dust grains into small dust grains in star-forming regions can produce similar effects in the IR SED.

These four mechanisms are likely to affect, with various degrees of relevance, the behavior of the $L(24)$–$L(\mathrm{Pa}\alpha)$ correlation in regions drawn from uniform samples (e.g., H II regions). A fifth mechanism:

5. the contribution of stellar populations of all ages to the IR emission as discussed and quantified in Appendix A;

becomes important when considering regions across different scales, e.g., samples that contain mixes of H II regions, galactic regions, and entire galaxies.

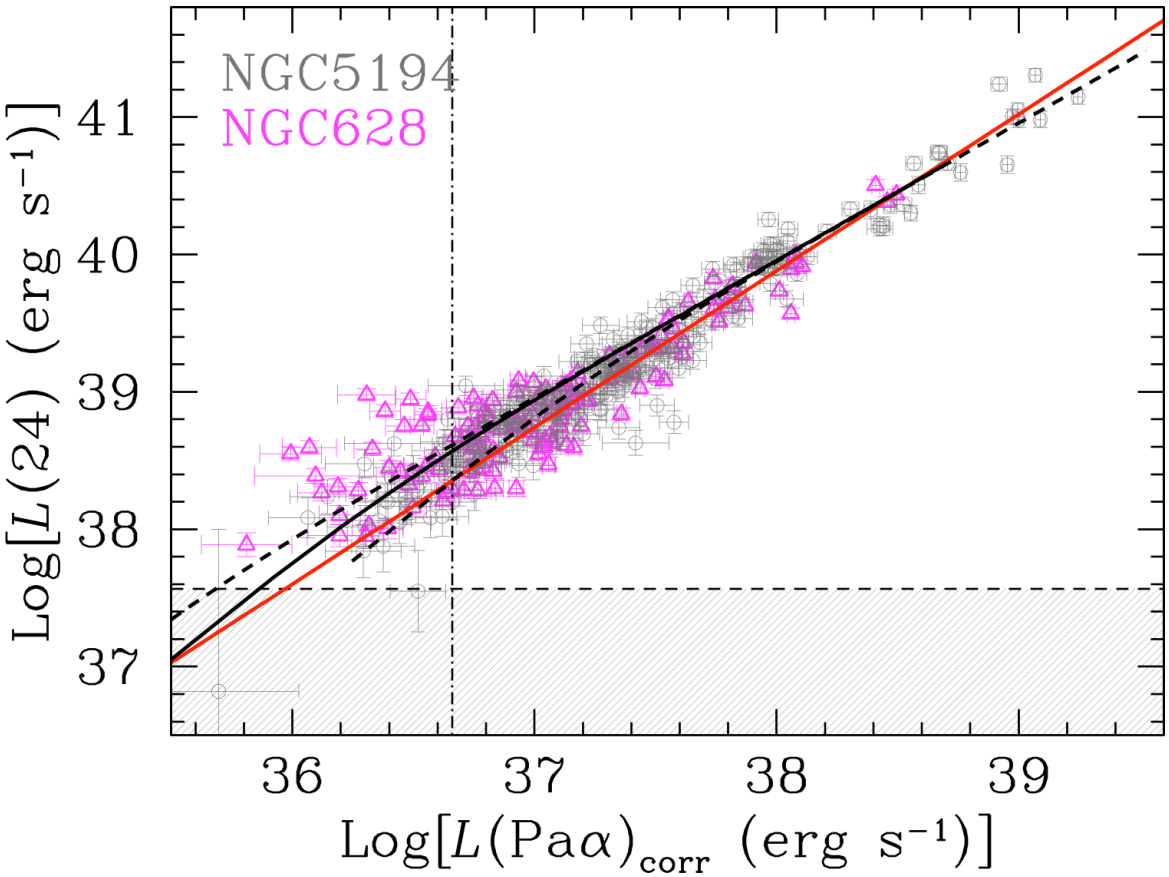

Figure 10. The 24 μm luminosity as a function of the attenuation-corrected Paα luminosity for the H II and giant H II regions in NGC 5194 (gray empty circles) and the H II regions in NGC 628 (magenta empty triangles) with their 1σ uncertainties. The horizontal dashed line and gray region show the location of the 5σ threshold at 24 μm in NGC 5194. The best-fit line to the cumulative sample of both galaxies is shown in blue. The 3 Myr model from Appendix B is shown as a black solid line; larger values of both luminosities correspond to larger values of the color excess $E(B-V)$, from 0.05 mag to 5 mag. Black dashed lines mark the 90% scatter in the $E(B-V)$–$L(\mathrm{Pa}\alpha)_{\mathrm{corr}}$ relation from Figure 3. Limiting the maximum $E(B-V)$ to 3 mag would decreases the maximum $L(\mathrm{Pa}\alpha)_{\mathrm{corr}}$ in each model by 0.37 dex.

We use the models from Appendix B to compare the best fit through the $L(24)$–$L(\mathrm{Pa}\alpha)_{\mathrm{corr}}$ measurements of H II regions in NGC 5194 and NGC 628 with the expected model trend from the first mechanism listed above. The model is shown in Figure 10 as the black lines, to be compared with the best-fit line (in log–log space) through the data. The two, model and best fit, follow each other closely, well within the scatter in the data, suggesting that even a simplified model like the one in Appendix B is sufficient to explain the superlinear relation between $L(24)$ and $L(\mathrm{Pa}\alpha)_{\mathrm{corr}}$. Although only suggestive, the data appear to continue along a trend with slope >1 at high luminosity, $L(\mathrm{Pa}\alpha)_{\mathrm{corr}} > 10^{38}$ erg s^{-1}, while the model converges to a slope $=1$. If confirmed by future H II region data at higher luminosity than currently available, some of the other mechanisms listed above, such as the increase in the $L(24)/L(\mathrm{IR})$ fraction, direct dust absorption of ionizing photons, and/or ionizing photon leakage are required as secondary effects to keep the slope superlinear. M. Relaño et al. (2013), for instance, find a weak trend of increasing $L(24)/L(\mathrm{IR})$ for increasing Hα surface brightness in the H II regions of M33.

The comparison between H II regions and ~0.5 kpc regions discussed in Section 4.2 is extended here to include larger regions and whole galaxies, using the data from the literature introduced in Section 5.1. Figure 11 shows that the combined data from all samples mark a fairly tight correlation across more than 5 orders of magnitude in Paα luminosity and more than 6 orders of magnitude in the 24 μm luminosity. The correlation is not surprising since luminosities are always correlated with each other, especially when systems at different distances are included. However, it is interesting that the correlation remains superlinear. The left panel shows the individual samples with different colors and symbols, together with several fitting relations from the literature, as indicated in the caption. The selected fitting relations are all nonlinear (slope >1 in log–log scale), except for the linear relation by G. H. Rieke et al. (2009), which applies to galaxies with $L(24) > 10^{42.6}$ erg s^{-1} and becomes nonlinear at $L(24) > 10^{43.7}$ erg s^{-1}. Most nonlinear fits published in the literature do provide a reasonable representation of the data, provided they are kept within their range of validity (Figure 11, left).

A single line fit through all data above the stochastic IMF sampling limit (596 points) gives

$$\mathrm{Log}[L(24)] = (1.23 \pm 0.01)\mathrm{Log}[L(\mathrm{Pa}\alpha_{\mathrm{corr}})] - (6.81 \pm 0.42), \quad (11)$$

with scatter $=0.14$ dex, where both $L(24)$ and $L(\mathrm{Pa}\alpha)_{\mathrm{corr}}$ are in units of erg s^{-1}. Figure 11, right, shows the best-fit line in comparison with the data from the combined sample now separated into the same three subsamples of Figure 8, right: H II regions (gray), galactic regions (cyan), and whole galaxies (magenta). The fit aligns well with the binned averages along the sample, also shown in the figure. The best-fit slope, with a

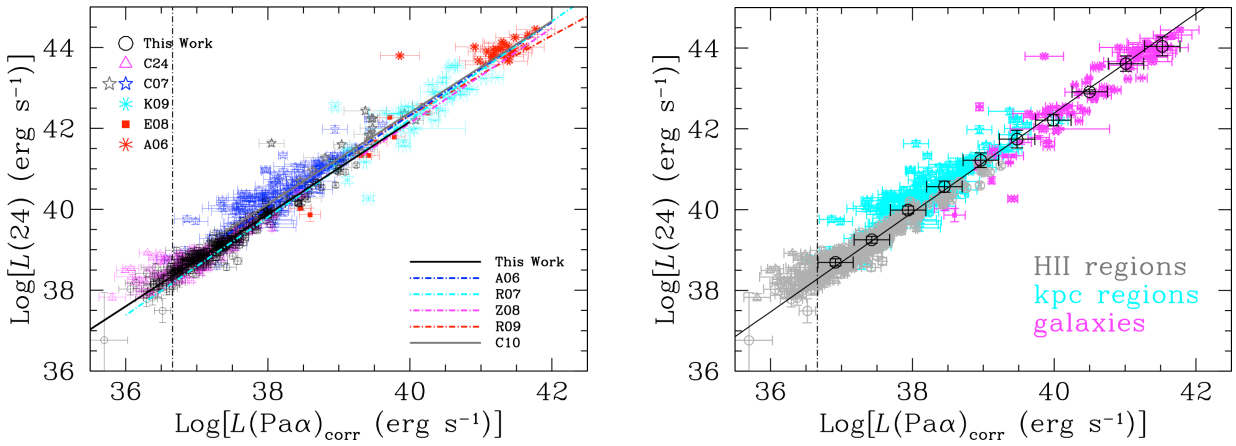

Figure 11. Left: the 24 μm luminosity as a function of the attenuation-corrected Paα luminosity for the same samples as those of Figure 8, left. All data are shown with 1σ uncertainties. The transition luminosity above which stochastic sampling of the IMF is mitigated is shown as a vertical dotted–dashed line. Several fits from previous authors are shown for comparison, using, for each relation, its range of validity: A. Alonso-Herrero et al. (2006, blue dotted–dashed line, denoted A06), M. Relaño et al. (2007, cyan dotted–dashed line, denoted R07), Y.-N. Zhu et al. (2008, magenta dotted–dashed line, denoted Z08), G. H. Rieke et al. (2009, red dotted–dashed line, denoted R09), and D. Calzetti et al. (2010, gray solid line, denoted C10), in addition to the one derived in this work (black solid line, denoted this work, Equation (2) with 21 μm replaced by 24 μm). Right: the same data as in the left panel, with the binned averages for all data above the stochastic IMF sampling limit (vertical dotted–dashed line). Different colors identify subsamples: H II regions (gray symbols), galactic regions (cyan symbols), and galaxies (magenta symbols). The binned averages are indicated as empty black circles with 1σ uncertainties. The best linear fit for all samples in log–log space, across over 5 orders of magnitude in Paα luminosity, is shown as a black line.

value of 1.23, is 4σ higher than the one for H II regions alone (slope = 1.14), also confirmed by a random drawing test (Appendix C), and is likely capturing the fact that larger regions and whole galaxies include IR emission that is not due to young star-forming regions. The added contribution to $L(24)$ thus increases for increasing luminosity, producing the super-linear slope.

Comparisons with models of different ages and durations from Appendix B confirm this speculation; the models follow the data reasonably well, both in the case of luminosity surface densities and of luminosities (Figure 12, left and right panels, respectively). The models, a 3 Myr old instantaneous burst population, and two models for constant star formation, at 100 Myr and 10 Gyr, are taken as representative of $\Sigma(24)$–$\Sigma(\mathrm{Pa}\alpha)_{\mathrm{corr}}$ trends for the subsamples of H II regions, galactic regions, and galaxies, respectively. These models highlight that the differences observed in the data are real (Figure 4, right, and Figure 12, left): galactic regions and galaxies have, on average, larger values of $\Sigma(24)$ at a given $\Sigma(\mathrm{Pa}\alpha)_{\mathrm{corr}}$. Figure 12, right, shows the same models scaled by the characteristic size of each subsample: 0.1 kpc for H II regions, 1 kpc for galactic regions, and 10 kpc for galaxies, to compare them with luminosities. The models line up with the data in their respective subsample and with each other, resulting in a slope > 1 and larger than the average slope of each individual model. In summary, one mechanism, the one for which low-luminosity regions are more transparent than higher-luminosity ones, can already explain much of the nonlinearity in the observed $L(24)$–$L(\mathrm{Pa}\alpha)$ relation. When linking together models of populations with different τ, the contribution of the IR emission from the low-mass stars pushes the relation to even steeper slopes, in agreement with observations.

We refrain from drawing additional conclusions from those models, as they were created with a number of simplified assumptions. One example of their limitations is the apparent agreement between the luminous IR galaxies and the 10 Gyr model, both in $\Sigma(24)$–$\Sigma(\mathrm{Pa}\alpha)_{\mathrm{corr}}$ and $L(24)$–$L(\mathrm{Pa}\alpha)_{\mathrm{corr}}$. Luminous IR galaxies have been shown to have younger average stellar populations and different IR SEDs from normal star-forming galaxies (e.g., A. Alonso-Herrero et al. 2006; D. Marcillac et al. 2006; G. H. Rieke et al. 2009; J. H. Howell et al. 2010; M. Pereira-Santaella et al. 2015; C. Cortijo-Ferrero et al. 2017; E. D. Paspaliaris et al. 2021). Thus, their agreement with the 10 Gyr model, generated to describe normal star-forming galaxies, highlights the degeneracies intrinsic to the models. A future dedicated analysis to this and similar samples may reveal the source of this inconsistency. Despite discrepancies, however, the data distribute fairly symmetrically about the best-fit line (Equation (11)), yielding a Log(SFR) prediction with a 1σ standard deviation of 0.19 dex across the full luminosity range (Appendix D).

Equation 11 translates into the following SFR calibration at 24 μm:

$$\mathrm{SFR}(24) = (1.466 \pm 0.508) \times 10^{-35} L(24)^{(0.8130 \pm 0.0066)} \quad \text{for} \quad 10^{38} \lesssim L(24) \lesssim 3 \times 10^{44}. \tag{12}$$

The calibration of M. Relaño et al. (2007) is close to the one above, predicting about 20% (46%) higher SFRs at the lowest (highest) luminosity in the validity range. Given the approximately symmetric dispersion of the data about the best fit, the above calibration will generally yield accurate values of the SFR within 55% (Appendix D), corresponding to a half-width at half maximum of 66%, across the full 24 μm luminosity range from H II regions to entire galaxies at solar metallicity.

Unlike $b(\tau)$, SFR(24) depends strongly on metallicity (e.g., D. Calzetti et al. 2007, 2010), due to the fact that galaxies become more transparent for decreasing metal (and dust) content. Thus, use of IR SFR indicators is generally not recommended for use in subsolar or low-dust systems. In these cases, a hybrid SFR indicator is preferable.

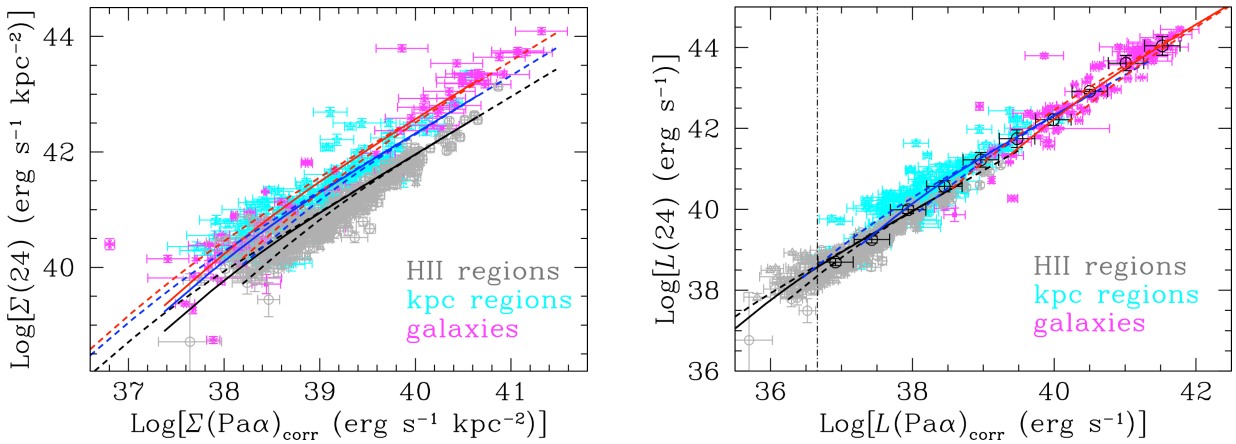

Figure 12. Left: the luminosity surface densities at 24 μm and at Paα_{corr} for the three subsamples of H II regions (gray symbols), galactic regions (cyan symbols), and galaxies (magenta symbols), with their 1σ uncertainties, are compared with the models of Appendix B. The models are a 3 Myr old instantaneous burst of star formation (black lines), and constant star formation with 100 Myr (blue lines) and 10 Gyr (red lines) durations, respectively. The dashed lines are the same as those in Figure 10. Data and models both show similar increases in Σ(24) at constant Σ(Paα)$_{corr}$, as expected if H II regions, galactic regions, and galaxies mark a progression in star formation duration. Right: the same as the left panel, but for luminosities. The model's luminosity surface densities are changed to luminosities using a characteristics spatial scale associated to each model (see text). The shifted models line up to mimic a linear relation with slope > 1, as observed.

6. Summary and Conclusions

We have combined new JWST/NIRCam and MIRI observations of the Paα nebular line and the 21 μm dust continuum of the nearby galaxy NGC 5194 to quantify the calibration of the mid-IR as an SFR indicator for H II regions, after correcting the Paα emission for dust attenuation. To expand on our results, we have joined the 254 H II regions of NGC 5194 with the 143 H II regions of NGC 628 analyzed by D. Calzetti et al. (2024), finding that Log[L(21)]–Log[L(Paα)] is linear with a slope > 1. We have also found that the scaling factor b for the hybrid [L(Hα) + bL(24)] SFR indicator is a factor of $\sim$4.4 larger in H II regions than in galaxies. Our samples of H II regions explicitly include regions ionized by single star clusters to ensure that a single (young) system contributes to both the ionized and IR emission. However, we also find that adding giant H II regions ionized by a group of star clusters to our H II region sample does not change the overall results. Applying models of stellar populations with different SFHs to our H II regions sample as well as published samples of $\sim$kiloparsec-sized galaxy regions and whole galaxies observed with Spitzer, we determine the following.

1. The relation Log[L(24)]–Log[L(Paα)] steepens when expanding the sample from H II regions only to H II regions + kiloparsec regions + galaxies, with the slope changing from a value of 1.14–1.23 (Equations (2) and (11)). The models show this is consistent with two mechanisms acting on the luminosities: (1) lower-luminosity regions are less attenuated by dust, with a larger fraction of their emission emerging directly at UV–optical wavelengths, driving the superlinear slope within homogeneous samples (e.g., H II regions only); and (2) larger physical regions correspond to longer durations of star formation, which increases the contribution of progressively more evolved stars to the IR emission, and produces a second steepening of the correlation when including mixed samples (H II regions + kiloparsec regions + galaxies).
2. The result for the H II regions + kiloparsec regions + galaxies sample translates into SFR $\propto L(24)^{\alpha}$ with the exponent $\alpha = (0.8130 \pm 0.0066)$. The scatter of the data about the mean trend indicates that SFRs derived with Equation (12) have a 1σ standard deviation of 55%. This calibration is recommended when using a single-band SFR indicator for metal-rich sources.
3. The scaling factor b for the hybrid SFR indicator depends on the duration of the star formation τ, if physically larger regions are associated with longer durations. The factor b decreases for progressively longer durations, as expected if mechanism (2) above is taken into account. An analytical expression for $b = b(\tau)$ is given in Equation (10), and should be relatively insensitive to metallicity variations. Studies that derive SFRs from hybrid tracers should include timescale-dependent values of b in their derivations.

These results cover 6 orders of magnitude in 24 μm luminosity, from 10^{38} erg s^{-1} to 3×10^{44} erg s^{-1}, with over 600 data points spanning H II regions, kiloparsec-sized galaxy regions, and whole galaxies, but are limited to solar metallicity systems. Future analyses will need to include subsolar metallicity systems to generalize the results presented in this work.

Acknowledgments

This work is based on observations made with the NASA/ESA/CSA James Webb Space Telescope and retrieved from the Mikulski Archive for Space Telescopes at the Space Telescope Science Institute, which is operated by the Association of Universities for Research in Astronomy, Inc., under NASA contract NAS 5-03127. These observations are associated with GO programs 1783 and 3435. The work also made use of archival data from the NASA/ESA Hubble Space Telescope obtained from the Space Telescope Science Institute, which is operated by the Association of Universities for Research in Astronomy, Inc., under NASA contract NAS 5-26555. HST data were retrieved from the Mikulski Archive for Space Telescopes at the Space Telescope Science Institute. Support for programs GO-1783 and GO-3435 was provided by

NASA through grants from the Space Telescope Science Institute.

V.B. and B.G. acknowledge partial support from grant JWST-GO-01783. D.D. and K.S. acknowledge partial support from grant JWST-GO-03435. A.A. acknowledges support from the Swedish National Space Agency (SNSA) through grant 2021-00108. A.D.C. acknowledges the support from the Royal Society University Research Fellowship URF/R1/191609. M.R.K. acknowledges support from the Australian Research Council through Laureate Fellowship FL220100020. R.S.K. acknowledges financial support from the European Research Council via the ERC Synergy Grant "ECOGAL" (project ID 855130), from the German Excellence Strategy via the Heidelberg Cluster of Excellence (EXC 2181 - 390900948) "STRUCTURES," and from the German Ministry for Economic Affairs and Climate Action in project "MAINN" (funding ID 50OO2206). R.S.K. also thanks the Harvard–Smithsonian Center for Astrophysics and the Radcliffe Institute for Advanced Studies for their hospitality during his sabbatical, and the 2024/25 Class of Radcliffe Fellows for highly interesting and stimulating discussions. M.M. acknowledges financial support through grants PRIN-MIUR 2020SKSTHZ, the INAF GO Grant 2022 "The revolution is around the corner: JWST will probe globular cluster precursors and Population III stellar clusters at cosmic dawn," and by the European Union – NextGenerationEU within PRIN 2022 project n.20229YBSAN - "Globular clusters in cosmological simulations and lensed fields: from their birth to the present epoch". M.R. acknowledges support from project PID2023-150178NB-I00 financed by MCIU/AEI/10.13039/501100011033, and by FEDER, UE.

The specific MAST observations analyzed in this work can be accessed via doi:10.17909/jp5q-s259.

This research has made use of the NASA/IPAC Extragalactic Database, which is funded by the National Aeronautics and Space Administration and operated by the California Institute of Technology.

Facility: JWST (NIRCam, MIRI), NED.

Software: JWST Calibration Pipeline (P. Greenfield & T. Miller 2016; H. Bushouse et al. 2022), Drizzlepac (S. Gonzaga et al. 2012; STSCI Development Team), IRAF (D. Tody 1986, 1993), SAOImage DS9 (W. A. Joye & E. Mandel 2003), Fortran.

Appendix A
Modeling the Light Absorbed by Dust in Stellar Populations

We model the scaling factor b from Equation (8) using stellar population models with extended SFHs, as opposed to the instantaneous star formation used in Section 4.3. Extended SFHs provide a better representation of the stellar populations in galaxies and large galaxy regions. Although they are not appropriate for H II regions, we argue in Section 5.1 that the average behavior of large samples of H II regions across a range of ages is comparable to the behavior of constant star formation over durations $\tau \lesssim 6$ Myr. With this similarity, we can connect our results for H II regions to the larger-region results.

We employ the Starburst99 models (C. Leitherer et al. 1999; G. A. Vázquez & C. Leitherer 2005) to generate SEDs with three separate SFHs: (1) constant star formation; (2) exponentially decreasing star formation with an e-folding time of ∼4.8 Gyr to emulate the decrease of the cosmic SFR from redshift $z \sim 2$ to today (P. Madau & M. Dickinson 2014); and (3) exponentially increasing star formation with an e-folding time of 4.3 Gyr, to represent galaxies like NGC 5194, which has culminated in a burst of star formation about 1 Gyr ago (E. E. Martínez-García et al. 2018). The SEDs are generated with star formation duration τ in the range 1 Myr–10 Gyr, using Padova AGB evolutionary tracks (L. Girardi et al. 2000) with metallicity $Z = 0.02$ (solar) and a P. Kroupa (2001) IMF in the stellar mass range 0.1–120 $M_\odot$. The attenuation curve of D. Calzetti et al. (2000) is used to generate dust-attenuated stellar SEDs. In order to apply different values of the dust color excess $E(B-V)$ to populations of different ages, the SEDs are "sliced" in bins of time: 1–3 Myr, 3–5 Myr, 5–10 Myr, 10–20 Myr, 20–50 Myr, 50–100 Myr, 100–200 Myr, 200–500 Myr, 500–700 Myr, 700 Myr–1 Gyr, 1–2 Gyr, 2–3 Gyr, 3–5 Gyr, 5–7 Gyr, and 7–10 Gyr. The goal is to simulate a decrease in dust attenuation as a stellar population ages, while using high values of the color excess ($E(B-V) = 1$ mag) for the youngest stellar populations. The unattenuated and dust-attenuated SEDs are then subtracted from each other to calculate the amount of light absorbed by dust within each time bin. These contributions are finally added together between 0 Myr and a maximum age to derive L(IR) as a

Table 7
Stellar Population Models with Dust Absorption

Parameter	Value	Range	Comments
SFH[a]	Constant	1 Myr–10 Gyr	⋯
	Decreasing	1 Myr–10 Gyr	e-folding $t = 4.8$ Gyr
	Increasing	1 Myr–10 Gyr	e-folding $t = 4.3$ Gyr
$E(B-V)$ (mag)[b]	Constant	0.1, 0.3, 0.5, 1.0	⋯
	Decreasing	1.0–0.3	⋯
	Decreasing	1.0–0.1	⋯
$L(\mathrm{H}\alpha)$[c]	100% Clustered	⋯	⋯
	50% Clustered, 50% Diffuse		
$L(24)/L(\mathrm{IR})$[d]	Constant	0.14	⋯
	Decreasing	0.30–0.10	⋯

Notes.
[a] The SFH of the models include three cases: constant star formation (Constant), exponentially decreasing star formation with a 4.8 Gyr e-folding time (Decreasing), and exponentially increasing SFH with a 4.3 Gyr e-folding time (Increasing). The star formation duration of each model spans the range 1 Myr–10 Gyr.
[b] The color excess, $E(B-V)$, applied to the population SEDs. Constant $E(B-V)$ values at all ages are only applied to the constant SFH model. $E(B-V)$ values that decrease for increasing age of the stellar population are applied to all three SFHs; two values for the minimum $E(B-V)$ are considered: 0.3 mag and 0.1 mag.
[c] The Hα luminosity is attenuated by $E(B-V) = 1.0$, i.e., the value of stellar populations younger than 10 Myr, for the 100% clustered emission case; for the 50% clustered, 50% diffuse case, half of the Hα emission is attenuated by $E(B-V) = 1.0$ and the remaining half has the same color excess of the oldest stellar population at the specified τ.
[d] Fraction of IR emission emerging at 24 μm. This fraction is adopted to be either constant at all ages or slightly decreasing from 0.3 at ages ⩽ 5 Myr to 0.10 at ages > 7 Gyr.

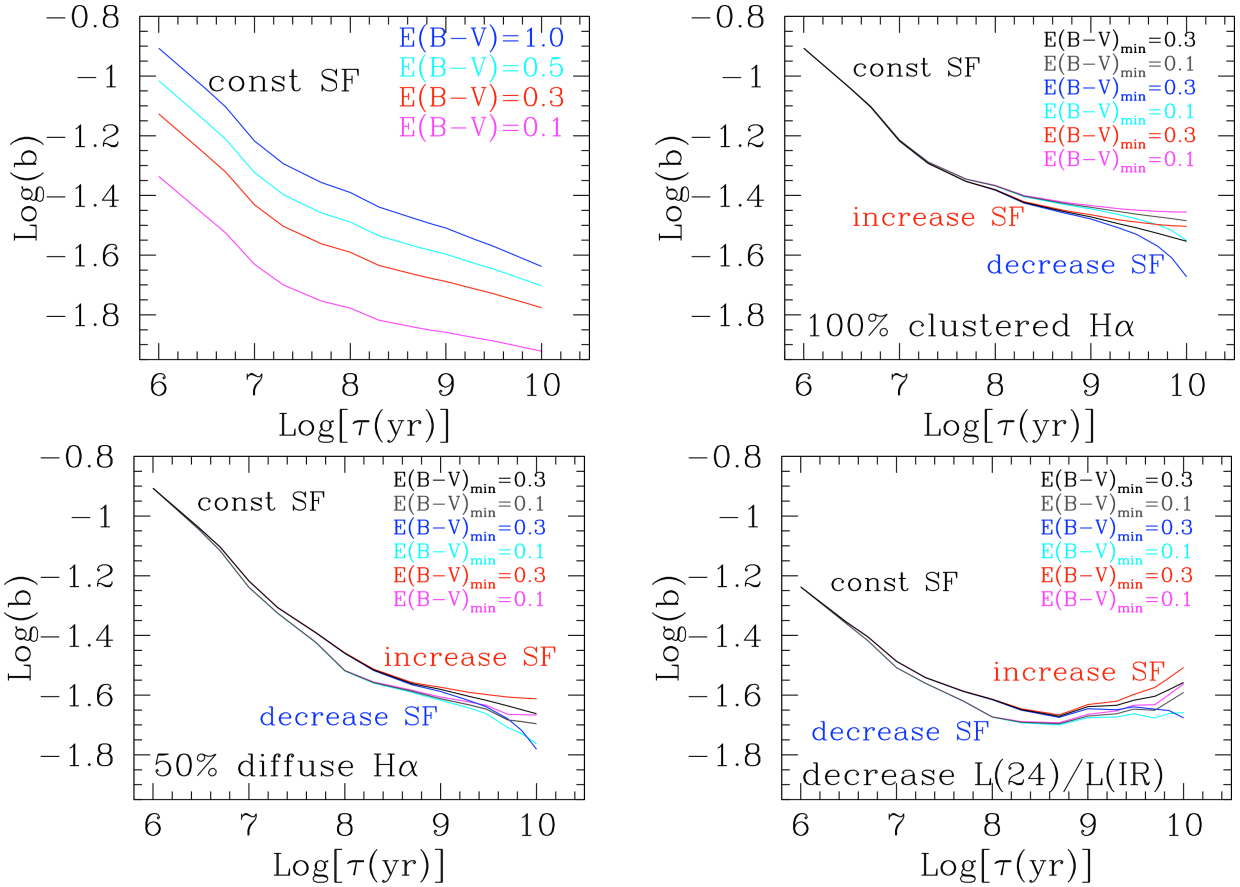

Figure 13. Top left: the scaling factor b as a function of the star formation duration τ, for constant star formation and a constant value of the color excess at all ages (Table 7); four values of $E(B-V)$ are shown as examples. Top right: the same as the top-left plot, but for the three SFHs of Table 7 and decreasing values of the color excess applied to population bins of increasing age; the Hα emission is attenuated by a constant $E(B-V)_{\rm gas}=1$ mag, the same color excess of the stellar populations $\lesssim$5 Myr. The SFHs are constant (black and gray lines), decreasing (blue and cyan lines), and increasing (red and magenta lines) star formation. Bottom left: same models as the top-right panel, but now the Hα attenuation is split into two components: 50% of the line emission at attenuated with $E(B-V)_{\rm gas}=1.0$ mag and the remaining 50% has the color excess of the oldest population. Bottom right: the same models as the bottom-left panel, but adding a decreasing fraction of the IR emission emerging at 24 μm for increasing age.

function of the duration τ of star formation. We assume energy balance, meaning that L(IR) is equal to the difference between the unattenuated and dust-attenuated SEDs. We also include the simplest case of constant star formation attenuated by a single value of $E(B-V)$ at all ages for illustrative purposes.

We model the Hα luminosity considering two cases: (1) the Hα is attenuated by same color excess as the youngest ($\lesssim$5 Myr) stellar populations, i.e., $E(B-V)=1.0$ mag; and (2) 50% of Hα has the same attenuation of the young ($\lesssim$5 Myr) stellar population with the remaining 50% assigned the attenuation of the oldest stellar population. The first model simulates the case that all the ionized gas emission is associated with the most recent star formation, while the second model simulates the presence of 50% clustered lines emission and 50% diffuse ionized gas (e.g., R. J. Reynolds 1984, 1990; A. M. N. Ferguson et al. 1996; C. G. Hoopes et al. 1996; C. G. Hoopes & R. A. M. Walterbos 2003; E. S. Voges & R. A. M. Walterbos 2006; M. S. Oey et al. 2007; K. Zhang et al. 2017).

Finally, we also consider two cases for the fraction of L(IR) emerging at 24 μm: (1) a constant value, 0.14, at all ages (G. H. Rieke et al. 2009; D. Calzetti et al. 2010), and (2) a decreasing fraction from 0.3 at ages <5 Myr to 0.10 at ages >7 Gyr, thus covering the full range of both H II regions (M. Relaño et al. 2013) and galaxies (G. H. Rieke et al. 2009; D. Calzetti et al. 2010). The latter model attributes hotter dust to younger stellar populations, which have both higher ionizing photon flux and nonionizing UV emission, and therefore potentially a higher $L(24)/L(\rm IR)$ fraction (D. A. Dale & G. Helou 2002; B. T. Draine et al. 2007). Table 7 lists the models used in this work and shown in Figure 13.

These models are more sophisticated than the simple assumptions used in D. Calzetti et al. (2024) in that they include three different SFHs, decreasing extinctions for increasing ages, and a more flexible implementation of both the attenuation at Hα and the fraction of IR emission emerging at 24 μm. Yet the basic result is similar to the findings by those authors: the scaling factor b decreases for increasing duration of the star formation, for a large range of assumptions (Figure 13). The reason for this behavior is straightforward: while the Hα emission is contributed by regions younger than $\sim$6 Myr, the IR emission is contributed by stellar populations of all ages, as discussed in the introduction. As the stellar population ages, it accumulates low-mass stars, which contribute to the heating of the dust, but not to the ionizing photon flux.

The panels in Figure 13 describe increasingly complex assumptions from top left to bottom right, providing a sense for how b changes for changing parameters, but also

highlighting the many degeneracies that characterize such modeling. In fact, different assumptions can be combined together to reproduce the observed trend of b with the duration of star formation. This implies that we cannot draw solid conclusions as to the SFH, dust content, etc., of the galaxies under consideration by simply looking at the values of b.

The results in Section 5.1 are discussed using as reference the models shown in the bottom-left panel of Figure 13. These models provide a representative description of the physical and geometrical conditions of nearby galaxies, in terms of the treatment of the attenuation of the stellar continuum and of the nebular lines.

Appendix B
Modeling the Correlation between Infrared and Ionized Gas Emission

The SED models introduced in the previous appendix can be used also to model the observed correlation between $L(24)$ and $L(\mathrm{Pa}\alpha)$. We restrict our attention to two of the five mechanisms listed in Section 5.2: (1) regions of low luminosity are more transparent than high luminosity regions; and (5) the increasing contribution of low-mass stars to the IR emission for increasing durations τ of the star formation, already discussed in Appendix A.

We use here instantaneous and constant star formation SEDs attenuated by the starburst attenuation curve to evaluate the impact of both mechanisms on the resulting relation between the luminosity surface densities at 24 μm and in the Paα light. Figure 14, left, shows the fraction of bolometric light from a stellar population absorbed by dust and reemitted in the IR as a function of color excess for three star formation models: a 3 Myr old instantaneous burst and constant star formation with durations of 100 Myr and 10 Gyr, respectively. Constant star formation with $\tau = 3$ Myr is indistinguishable from the 3 Myr old instantaneous model. The range of color excess shown in the figure spans 0–2 mag, as the IR fraction of the bolometric light quickly approaches unity for all three SEDs for larger $E(B-V)$ values. The differences in the asymptotic approach of the three SEDs quantify the effect of the increasing contribution of lower-mass stars to the bolometric luminosity for increasing τ. These lower-mass stars mainly contribute to the optical–near-infrared emission, which is less sensitive to the effects of dust attenuation than the UV light; thus their presence delays the approach to the asymptotic value of unity of the $L(\mathrm{IR})/L(\mathrm{bol})$ ratio. The trends are only minimally affected by the choice of attenuation/extinction curve. This is shown in Figure 14, left, for the $\tau = 100$ Myr model, where the $L(\mathrm{IR})/L(\mathrm{bol})$ versus $E(B-V)$ trend for our default choice, the starburst attenuation curve, is compared with the analogous trends when using the Milky Way, Large Magellanic Cloud, and Small Magellanic Cloud extinction curves (E. L. Fitzpatrick 1999; K. D. Gordon et al. 2003; E. L. Fitzpatrick & D. Massa 2007; E. L. Fitzpatrick et al. 2019). For $E(B-V) > 0.15$ mag, the differences in the $L(\mathrm{IR})/L(\mathrm{bol})$ ratio are <0.05 dex for any choice of the attenuation/extinction curve at a given SFH.

To convert the trend with color excess to a trend with ionized gas luminosity surface density, we use the empirical relation between $E(B-V)$ and the luminosity surface density $\Sigma(\mathrm{Pa}\alpha)_{\mathrm{corr}}$ derived by D. Calzetti et al. (2007) with a correction for a typo:

$$E(B-V) = 0.21\left(\frac{\Sigma_{\mathrm{ion}}}{1.433 \times 10^{51}}\right)^{0.61}, \quad \text{(B1)}$$

which is appropriate for metal-rich regions. With the updated relation, we obtain

$$\mathrm{Log}[E(B-V)] = -24.099 + 0.61\mathrm{Log}[\Sigma(\mathrm{Pa}\alpha_{\mathrm{corr}})], \quad \text{(B2)}$$

which fits the data in D. Calzetti et al. (2007), and has been used both for the tracks in Figure 3 (right) and in D. Calzetti et al. (2024). We combine this relation, and its 90% range, with the $L(\mathrm{IR})/L(\mathrm{bol})$ trend of Figure 14, left, for all three models shown, which result in the plot of Figure 14, right. In all models the ratio $L(24)/L(\mathrm{IR})$ is kept constant at the value

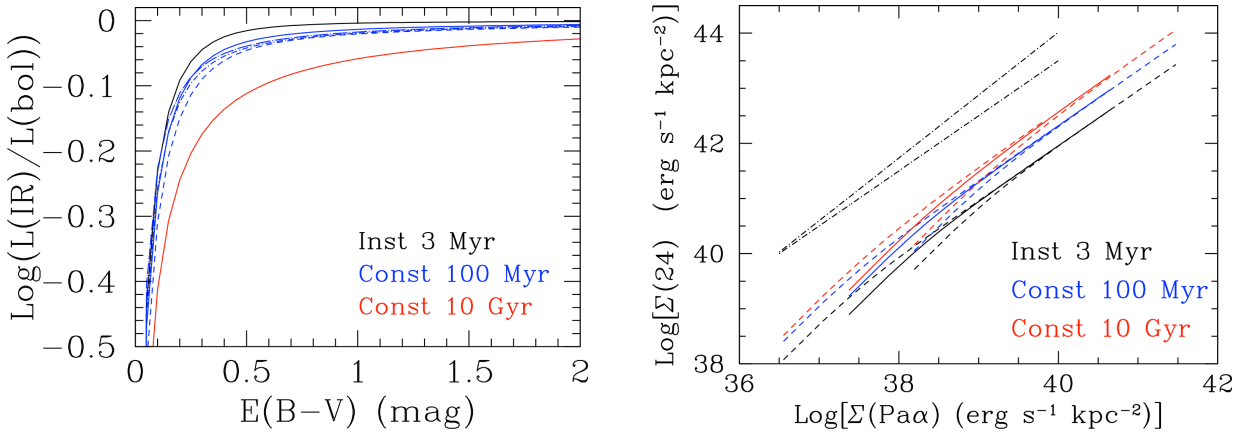

Figure 14. Left: the fraction of bolometric luminosity emerging in the IR, as a function of color excess $E(B-V)$, for the following stellar population models: 3 Myr old instantaneous burst (black solid line); constant star formation over 100 Myr (blue lines); and constant star formation over 10 Gyr (red solid line). The effect of different extinction/attenuation curve choices are shown for the 100 Myr constant star formation model: starburst attenuation curve (blue solid) and the Milky Way (blue dashed), Large Magellanic Cloud (blue short dotted–dashed), and Small Magellanic Cloud (blue long dotted–dashed) extinction curves. Right: the 24 μm luminosity surface density as a function of the extinction-corrected Paα luminosity surface density for the three star formation models described in the left panel. The Paα surface density is derived via the $E(B-V)$–$\Sigma(\mathrm{Pa}\alpha)$ relation in Equation (B2) (D. Calzetti et al. 2007). The models for the 3 Myr instantaneous burst (black solid line), $\tau = 100$ Myr constant star formation (blue solid line), and $\tau = 10$ Gyr constant star formation (red solid line) mark a sequence of increasing $\Sigma(24)$ at fixed $\Sigma(\mathrm{Pa}\alpha)_{\mathrm{corr}}$. The relation at each age is shown with the 90% scatter in the $E(B-V)$–Paα relation from D. Calzetti et al. (2007) as dashed lines. The black dotted–dashed straight lines are examples of linear relations with slopes (bottom to top) of 1 and 1.14, to provide a visual reference.

0.14. Despite the simplicity of our approach in terms of both SFH and attenuation recipe (all stellar populations are attenuated by the same color excess), we can already identify and quantify two important trends. The first is between the two surface densities: in each model, the 24 μm emission is underluminous at the lowest values of $\Sigma(\mathrm{Pa}\alpha)_{\mathrm{corr}}$ creating a nonlinear relation, with a slope > 1 in log–log scale. For reference, Figure 14, right, reports two straight lines: one with slope $= 1$ and one with slope $= 1.14$, the latter close to what we find for H II regions and what D. Calzetti et al. (2010) find for ∼kiloparsec-sized regions. In all cases, the Log[$\Sigma(24)$]–Log[$\Sigma(\mathrm{Pa}\alpha)_{\mathrm{corr}}$] relation has an asymptotic behavior toward a slope $= 1$, which is reached sooner for the youngest models (see Figure 14, left). The second trend is with increasing star formation duration τ: the longer τ the higher the value of $\Sigma(24)$ at fixed $\Sigma(\mathrm{Pa}\alpha)_{\mathrm{corr}}$, which mirrors the trends for b with τ presented in the previous appendix. Each model is shown for the range $E(B-V) = 0.05$–5 mag; restricting the range in color excess to 0.05–2 mag (0.05–3 mag) would lower the maximum $L(\mathrm{Pa}\alpha)$ of each model by 0.65 dex (0.37 dex). Finally, the impact of the 90% scatter in the $E(B-V)$ versus $\Sigma(\mathrm{Pa}\alpha)_{\mathrm{corr}}$ relation is shown in Figure 14, right, as dashed lines: the large scatter between $E(B-V)$ and Paα has a minimal impact on the predicted 24 μm luminosity surface density, and it mostly serves to increase the range for each model. We use these models in Section 5.2 to provide a comparison with observational data.

Appendix C
Histograms of Slopes and Intercepts

We test how effectively we can discriminate between the slopes of 1.14 ± 0.02 and 1.23 ± 0.01 found for the Log[$L(24)$] − Log[$L(\mathrm{Pa}\alpha)_{\mathrm{corr}}$] relations of H II regions (Equation (2)) and the full sample of H II regions, kiloparsec-size regions, and galaxies (Equation (11)), respectively. We produce 1000 realizations of each data point in each sample by randomly drawing numbers (M. Matsumoto & T. Nishimura 1998) within the data's 3σ uncertainties along both the x-axis and y-axis. Any assumption on the underlying distribution of the uncertainties is relaxed by adopting uniform priors. We perform a linear fit for each realization, and create histograms of the resulting slopes and intercepts for the two relations (Figure 15). The data centered around the slope $= 1.14$ (H II regions only) are consistent with a Gaussian distribution with standard deviation $\sigma = 0.017$, while the distribution centered on the slope $= 1.23$ (full sample) has standard deviation $\sigma = 0.0045$. For the intercepts, the Gaussian consistent with the distribution of the data for the H II regions sample has standard deviation $\sigma = 0.59$ and for the full sample the stadanrd deviation is $\sigma = 0.16$. Thus, even with a non-Gaussian distribution of uncertainties, the two relations can be discriminated to better than 4σ.

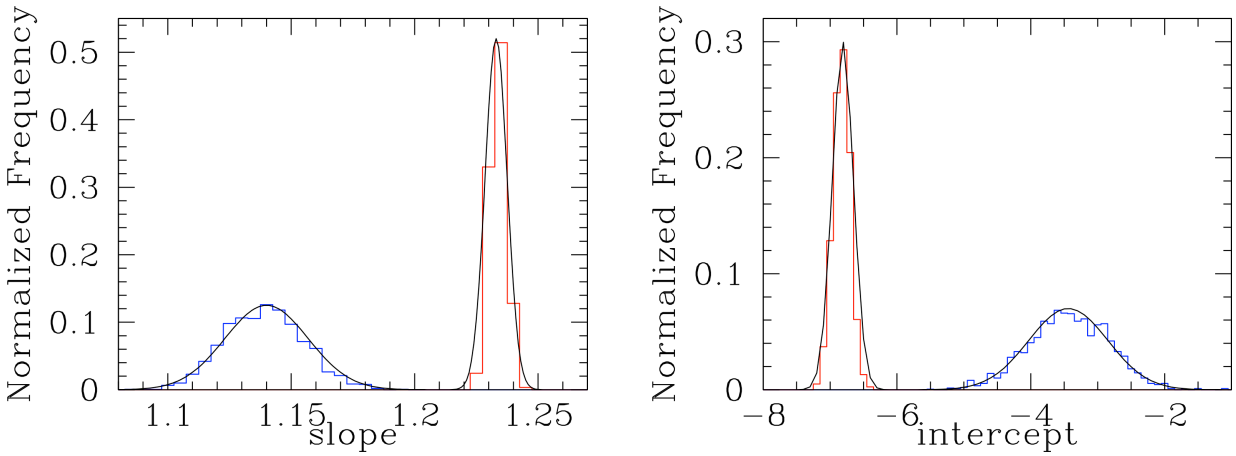

Figure 15. Histograms of the slope (left panels) and intercept (right panel) data for the H II region sample (blue) and the full sample of H II regions, kiloparsec-size regions, and galaxies (red), with Gaussian distributions overplotted on the histograms (black).

Appendix D
Scatter in the $L(24)$–$L(\mathrm{Pa}\alpha)$ Relation

Here we show the distribution of the observations about the mean fitted trend of Figure 11, right, which we express as scatter of the true SFR about the predicted SFR(24) from Equation (12) to facilitate evaluation of the uncertainties in this parameter. Figure 16 illustrates the distribution of $\mathrm{SFR}/\mathrm{SFR}_{\mathrm{fit}}$ for our entire sample of 658 sources, which includes H II regions, galaxy regions, and galaxies across the full luminosity range in the local Universe. In this figure, SFR is the true SFR derived from the attenuation-corrected Paα luminosity, while $\mathrm{SFR}_{\mathrm{fit}}$ is the predicted SFR from the 24 μm luminosity using Equation (12). Only data with a Paα luminosity above the stellar IMF stochastic sampling limit were used in the derivation of this equation (see main text for details). The left panel shows the distribution of individual sources about the best-fit line. The only notable deviation from a fairly symmetrical distribution is displayed by the faint end of the galaxy regions from the sample of D. Calzetti et al. (2007).

The right panel of Figure 16 shows a histogram of the data above the luminosity limit for stochastic IMF sampling, together with the best-fit Gaussian to the distribution. The excess in the tail at negative values ($\mathrm{SFR}/\mathrm{SFR}_{\mathrm{fit}} < 0.4$) is due to the same sources from the sample of D. Calzetti et al. (2007) discussed above. The standard deviation of the Gaussian is 0.19, which corresponds to a 1σ scatter in the $\mathrm{SFR}/\mathrm{SFR}_{\mathrm{fit}}$ ratio of 55%. We consider this scatter representative of the accuracy of Equation (12) in predicting the true SFR from the 24 μm luminosity from H II regions to luminous IR galaxies at solar metallicity in the local Universe.

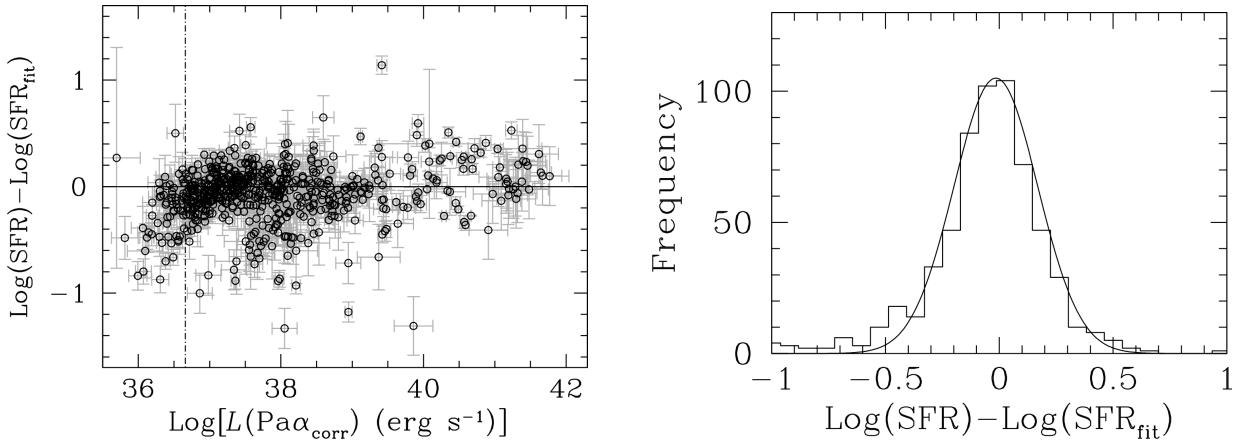

Figure 16. Left: the distribution of Log(SFR) for our full sample of H II regions, galaxy regions, and galaxies, relative to the predicted Log($\mathrm{SFR}_{\mathrm{fit}}$) from the best-fit line of Equation (12). The SFRs are calculated from the attenuation-corrected Paα luminosity. The vertical line marks the location of the luminosity below which the stellar IMF is stochastically sampled. Only sources above this limit where used in the derivation of the best-fit line. Right: a histogram of the data to the left with luminosity above the stochastic IMF sampling limit, shown with a best-fit Gaussian.

ORCID iDs

Daniela Calzetti https://orcid.org/0000-0002-5189-8004
Robert C. Kennicutt https://orcid.org/0000-0001-5448-1821
Angela Adamo https://orcid.org/0000-0002-8192-8091
Karin Sandstrom https://orcid.org/0000-0002-4378-8534
Daniel A. Dale https://orcid.org/0000-0002-5782-9093
Bruce Elmegreen https://orcid.org/0000-0002-1723-6330
John S. Gallagher https://orcid.org/0000-0001-8608-0408
Benjamin Gregg https://orcid.org/0000-0003-4910-8939
Varun Bajaj https://orcid.org/0009-0008-4009-3391
Torsten Böker https://orcid.org/0000-0002-5666-7782
Giacomo Bortolini https://orcid.org/0009-0003-6182-8928
Martha Boyer https://orcid.org/0000-0003-4850-9589
Matteo Correnti https://orcid.org/0000-0001-6464-3257
Ilse De Looze https://orcid.org/0000-0001-9419-6355
Bruce T. Draine https://orcid.org/0000-0002-0846-936X
Ana Duarte-Cabral https://orcid.org/0000-0002-5259-4774
Helena Faustino Vieira https://orcid.org/0000-0002-2199-0977
Kathryn Grasha https://orcid.org/0000-0002-3247-5321
L. K. Hunt https://orcid.org/0000-0001-9162-2371
Kelsey E. Johnson https://orcid.org/0000-0001-8348-2671
Ralf S. Klessen https://orcid.org/0000-0002-0560-3172
Mark R. Krumholz https://orcid.org/0000-0003-3893-854X
Thomas S.-Y. Lai https://orcid.org/0000-0001-8490-6632
Drew Lapeer https://orcid.org/0009-0009-5509-4706
Sean T. Linden https://orcid.org/0000-0002-1000-6081
Matteo Messa https://orcid.org/0000-0003-1427-2456
Göran Östlin https://orcid.org/0000-0002-3005-1349
Alex Pedrini https://orcid.org/0000-0002-8222-8986
Mònica Relaño https://orcid.org/0000-0003-1682-1148
Elena Sabbi https://orcid.org/0000-0003-2954-7643
Eva Schinnerer https://orcid.org/0000-0002-3933-7677
Evan Skillman https://orcid.org/0000-0003-0605-8732
Linda J. Smith https://orcid.org/0000-0002-0806-168X
Monica Tosi https://orcid.org/0000-0002-0986-4759
Fabian Walter https://orcid.org/0000-0003-4793-7880
Tony D. Weinbeck https://orcid.org/0009-0005-8923-558X

References

Adamo, A., Ryon, J. E., Messa, M., et al. 2017, ApJ, 841, 131
Adamo, A., Zeidler, P., Kruijssen, J. M. D., et al. 2020, SSRv, 216, 69
Alonso-Herrero, A., Rieke, G. H., Rieke, M. J., et al. 2006, ApJ, 650, 835
Asplund, M., Grevesse, N., Sauval, A. J., & Scott, P. 2009, ARA&A, 47, 481
Belfiore, F., Leroy, A. K., Williams, T. G., et al. 2023, A&A, 678, A129
Bendo, G. J., Boselli, A., Dariush, A., et al. 2012, MNRAS, 419, 1833
Berg, D. A., Pogge, R. W., Skillman, E. D., et al. 2020, ApJ, 893, 96
Boquien, M., Kennicutt, R., Calzetti, D., et al. 2016, A&A, 591, A6
Boselli, A., Lequeux, J., & Gavazzi, G. 2004, A&A, 428, 409
Bouwens, R., Gonzalez-Lopez, J., Aravena, M., et al. 2020, ApJ, 902, 112
Brown, G., & Gnedin, O. Y. 2021, MNRAS, 508, 5935
Buat, V., & Deharveng, J. M. 1988, A&A, 195, 60
Buat, V., Donas, J., Milliard, B., & Xu, C. 1999, A&A, 352, 371
Buat, V., & Xu, C. 1996, A&A, 306, 61
Bushouse, H., Eisenhamer, J., Dencheva, N., et al. 2022, JWST Calibration Pipeline v1.9.0, Zenodo, doi:10.5281/zenodo.7487203
Calzetti, D. 2001, PASP, 113, 1449
Calzetti, D. 2013, in Star Formation Rate Indicators, ed. J. Falcón-Barroso & J. H. Knapen (Cambridge: Cambridge Univ. Press), 419
Calzetti, D., Adamo, A., Linden, S. T., et al. 2024, ApJ, 971, 118
Calzetti, D., Armus, L., Bohlin, R. C., et al. 2000, ApJ, 533, 682
Calzetti, D., Kinney, A. L., & Storchi-Bergmann, T. 1994, ApJ, 429, 582
Calzetti, D., Kennicutt, R. C., Engelbracht, C. W., et al. 2007, ApJ, 666, 870
Calzetti, D., Kennicutt, R. C. J., Bianchi, L., et al. 2005, ApJ, 633, 871
Calzetti, D., Lee, J. C., Sabbi, E., et al. 2015, AJ, 149, 51
Calzetti, D., Wu, S. Y., Hong, S., et al. 2010, ApJ, 714, 1256
Casey, C. M., Zavala, J. A., Spilker, J., et al. 2018, ApJ, 862, 77
Cerviño, M., Valls-Gabaud, D., Luridiana, V., & Mas-Hesse, J. M. 2002, A&A, 381, 51
Chisholm, J., Rigby, J. R., Bayliss, M., et al. 2019, ApJ, 882, 182
Chomiuk, L., & Povich, M. S. 2011, AJ, 142, 197
Colombo, D., Meidt, S. E., Schinnerer, E., et al. 2014, ApJ, 784, 4
Cook, D. O., Dale, D. A., Johnson, B. D., et al. 2014, MNRAS, 445, 899
Cortijo-Ferrero, C., González Delgado, R. M., Pérez, E., et al. 2017, A&A, 607, A70
Croxall, K. V., Pogge, R. W., Berg, D. A., Skillman, E. D., & Moustakas, J. 2015, ApJ, 808, 42
Csörnyei, G., Anderson, R. I., Vogl, C., et al. 2023, A&A, 678, A44
Dale, D. A., Aniano, G., Engelbracht, C. W., et al. 2012, ApJ, 745, 95
Dale, D. A., Boquien, M., Turner, J. A., et al. 2023, AJ, 165, 260
Dale, D. A., Cohen, S. A., Johnson, L. C., et al. 2009, ApJ, 703, 517
Dale, D. A., & Helou, G. 2002, ApJ, 576, 159
Dayal, P., Ferrara, A., Sommovigo, L., et al. 2022, MNRAS, 512, 989
de la Fuente Marcos, R., & de la Fuente Marcos, C. 2009, ApJ, 700, 436
de Vaucouleurs, G., de Vaucouleurs, A., Corwin, H. G. J., et al. 1991, Third Reference Catalogue of Bright Galaxies (Berlin: Springer)
Dicken, D., Marín, M. G., Shivaei, I., et al. 2024, A&A, 689, A5
Dong, R., & Draine, B. T. 2011, ApJ, 727, 35
Dopita, M. A., Groves, B. A., Sutherland, R. S., & Kewley, L. J. 2003, ApJ, 583, 727
Draine, B. T. 2011, ApJ, 732, 100
Draine, B. T., Dale, D. A., Bendo, G., et al. 2007, ApJ, 663, 866
Efremov, Y. N., & Elmegreen, B. G. 1998, MNRAS, 299, 588
Egorov, O. V., Kreckel, K., Sandstrom, K. M., et al. 2023, ApJL, 944, L16
Elia, D., Evans, N. J., Soler, J. D., et al. 2025, ApJ, 980, 216
Elia, D., Molinari, S., Schisano, E., et al. 2022, ApJ, 941, 162
Elmegreen, B. G. 1989, ApJ, 338, 178
Elmegreen, B. G. 2011, in EAS Publications Ser. 51, ed. C. Charbonnel & T. Montmerle (Les Ulis: EDP Sciences), 31
Elmegreen, B. G. 2018, ApJ, 853, 88
Engelbracht, C. W., Rieke, G. H., Gordon, K. D., et al. 2008, ApJ, 678, 804
Fahrion, K., & De Marchi, G. 2023, A&A, 671, L14
Ferguson, A. M. N., Wyse, R. F. G., Gallagher, J. S. I., & Hunter, D. A. 1996, AJ, 111, 2265
Fitzpatrick, E. L. 1999, PASP, 111, 63
Fitzpatrick, E. L., & Massa, D. 2007, ApJ, 663, 320
Fitzpatrick, E. L., Massa, D., Gordon, K. D., Bohlin, R., & Clayton, G. C. 2019, ApJ, 886, 108
Fumagalli, M., da Silva, R. L., & Krumholz, M. R. 2011, ApJL, 741, L26
Gallagher, J. S., & Hunter, D. A. 1983, ApJ, 274, 141
Gardner, J. P., Mather, J. C., Abbott, R., et al. 2023, PASP, 135, 068001
Garn, T., & Best, P. N. 2010, MNRAS, 409, 421
Girardi, L., Bressan, A., Bertelli, G., & Chiosi, C. 2000, A&AS, 141, 371
Gonzaga, S., Hack, W., Fruchter, A., & Mack, J. 2012, The DrizzlePac Handbook, HST Data Handbook (Baltimore, MD: STScI)
Gordon, K. D., Clayton, G. C., Misselt, K. A., Land olt, A. U., & Wolff, M. J. 2003, ApJ, 594, 279
Gouliermis, D. A. 2018, PASP, 130, 072001
Gouliermis, D. A., Thilker, D., Elmegreen, B. G., et al. 2015, MNRAS, 452, 3508
Grasha, K., Calzetti, D., Adamo, A., et al. 2015, ApJ, 815, 93
Grasha, K., Calzetti, D., Adamo, A., et al. 2017a, ApJ, 840, 113
Grasha, K., Elmegreen, B. G., Calzetti, D., et al. 2017b, ApJ, 842, 25
Greenfield, P., & Miller, T. 2016, A&C, 16, 41
Gregg, B., Calzetti, D., & Heyer, M. 2022, ApJ, 928, 120
Hannon, S., Lee, J. C., Whitmore, B. C., et al. 2022, MNRAS, 512, 1294
Hao, C.-N., Kennicutt, R. C., Johnson, B. D., et al. 2011, ApJ, 741, 124
Helou, G. 1986, ApJL, 311, L33
Heyer, M., Krawczyk, C., Duval, J., & Jackson, J. M. 2009, ApJ, 699, 1092
Heyer, M. H., & Brunt, C. M. 2004, ApJL, 615, L45
Hirashita, H., Buat, V., & Inoue, A. K. 2003, A&A, 410, 83
Hoopes, C. G., & Walterbos, R. A. M. 2003, ApJ, 586, 902
Hoopes, C. G., Walterbos, R. A. M., & Greenwalt, B. E. 1996, AJ, 112, 1429
Howell, J. H., Armus, L., Mazzarella, J. M., et al. 2010, ApJ, 715, 572
Hunter, D. A., Gallagher, J. S., III, Rice, W. L., Gillett, F. C., et al. 1989, ApJ, 336, 152
Inoue, A. K., Hirashita, H., & Kamaya, H. 2001, ApJ, 555, 613
Isobe, T., Feigelson, E. D., Akritas, M. G., & Babu, G. J. 1990, ApJ, 364, 104
Joye, W. A., & Mandel, E. 2003, in ASP Conf. Ser. 295, Astronomical Data Analysis Software and Systems, ed. H. E. Payne, R. I. Jedrzejewski, & R. N. Hook (San Francisco, CA: ASP), 489

Kelly, B. C. 2007, ApJ, 665, 1489
Kennicutt, R. C., & Evans, N. J. 2012, ARA&A, 50, 531
Kennicutt, R. C. J., Calzetti, D., Walter, F., et al. 2007, ApJ, 671, 333
Kennicutt, R. C. J., Hao, C.-N., Calzetti, D., et al. 2009, ApJ, 703, 1672
Kennicutt, R. C. J., Lee, J. C., Funes, J. G., et al. 2008, ApJS, 178, 247
Knutas, A., Adamo, A., Pedrini, A., et al. 2025, arXiv:2505.08874
Kroupa, P. 2001, MNRAS, 322, 231
Krumholz, M. R., & Matzner, C. D. 2009, ApJ, 703, 1352
Leitherer, C., Schaerer, D., Goldader, J. D., et al. 1999, ApJS, 123, 3
Leroy, A. K., Sandstrom, K., Rosolowsky, E., et al. 2023, ApJL, 944, L9
Li, Y., Crocker, A. F., Calzetti, D., et al. 2013, ApJ, 768, 180
Libralato, M., Argyriou, I., Dicken, D., et al. 2024, PASP, 136, 034502
Liu, F.-Y., Dunlop, J. S., McLure, R. J., et al. 2025, arXiv:2503.07774
Liu, G., Koda, J., Calzetti, D., Fukuhara, M., & Momose, R. 2011, ApJ, 735, 63
Lonsdale Persson, C. J., & Helou, G. 1987, ApJ, 314, 513
Madau, P., & Dickinson, M. 2014, ARA&A, 52, 415
Magnelli, B., Lutz, D., Saintonge, A., et al. 2014, A&A, 561, A86
Marcillac, D., Elbaz, D., Chary, R. R., et al. 2006, A&A, 451, 57
Martínez-García, E. E., Bruzual, G., Magris, C. G., & González-López lira, R. A. 2018, MNRAS, 474, 1862
Matsumoto, M., & Nishimura, T. 1998, ATMCS, 8, 3
McCallum, L., Wood, K., Benjamin, R. A., et al. 2025, MNRAS, 540, L21
McQuinn, K. B. W., Skillman, E. D., Dolphin, A. E., Berg, D., & Kennicutt, R. 2016, ApJ, 826, 21
Meidt, S. E., Schinnerer, E., Knapen, J. H., et al. 2012, ApJ, 744, 17
Mendigutía, I., Lada, C. J., & Oudmaijer, R. D. 2018, A&A, 618, A119
Messa, M., Calzetti, D., Adamo, A., et al. 2021, ApJ, 909, 121
Meurer, G. R., Heckman, T. M., & Calzetti, D. 1999, ApJ, 521, 64
Moustakas, J., & Kennicutt, R. C., Jr. 2006, ApJS, 164, 81
Oey, M. S., Meurer, G. R., Yelda, S., et al. 2007, ApJ, 661, 801
Osterbrock, D. E., & Ferland, G. J. 2006, Astrophysics of Gaseous Nebulae and Active Galactic Nuclei (Mill Valley, CA: Univ. Science Books)
Paspaliaris, E. D., Xilouris, E. M., Nersesian, A., et al. 2021, A&A, 649, A137
Pedrini, A., Adamo, A., Bik, A., et al. 2025, arXiv:2509.01670
Pedrini, A., Adamo, A., Calzetti, D., et al. 2024, ApJ, 971, 32
Pellegrini, E. W., Oey, M. S., Winkler, P. F., et al. 2012, ApJ, 755, 40
Pereira-Santaella, M., Alonso-Herrero, A., Colina, L., et al. 2015, A&A, 577, A78
Press, W. H., Teukolsky, S. A., Vetterling, W. T., & Flannery, B. P. 1992, Numerical Recipes in FORTRAN. The Art of Scientific Computing (Cambridge: Cambridge Univ. Press)
Querejeta, M., Pety, J., Schruba, A., et al. 2023, A&A, 680, A4
Relaño, M., De Looze, I., Kennicutt, R. C., et al. 2018, A&A, 613, A43
Relaño, M., Lisenfeld, U., Pérez-González, P. G., Vílchez, J. M., & Battaner, E. 2007, ApJL, 667, L141
Relaño, M., Verley, S., Pérez, I., et al. 2013, A&A, 552, A140
Rémy-Ruyer, A., Madden, S. C., Galliano, F., et al. 2015, A&A, 582, A121
Renzini, A., & Peng, Y.-j. 2015, ApJL, 801, L29
Reynolds, R. J. 1984, ApJ, 282, 191
Reynolds, R. J. 1990, ApJL, 349, L17
Rieke, G. H., Alonso-Herrero, A., Weiner, B. J., et al. 2009, ApJ, 692, 556
Rieke, G. H., Wright, G. S., Böker, T., et al. 2015, PASP, 127, 584
Rieke, G. H., Young, E. T., Engelbracht, C. W., et al. 2004, ApJS, 154, 25
Rieke, M. J., Kelly, D., & Horner, S. 2005, Proc. SPIE, 5904, 1
Rieke, M. J., Kelly, D. M., Misselt, K., et al. 2023, PASP, 135, 028001
Rigby, J., Perrin, M., McElwain, M., et al. 2023, PASP, 135, 048001
Rowan-Robinson, M., & Crawford, J. 1989, MNRAS, 238, 523
Ryon, J. E., Bastian, N., Adamo, A., et al. 2015, MNRAS, 452, 525
Ryon, J. E., Gallagher, J. S., Smith, L. J., et al. 2017, ApJ, 841, 92
Sabbi, E., Calzetti, D., Ubeda, L., et al. 2018, ApJS, 235, 23
Sauvage, M., & Thuan, T. X. 1992, ApJL, 396, L69
Schlafly, E. F., & Finkbeiner, D. P. 2011, ApJ, 737, 103
Shashank, G., Subramanian, S., Muraleedharan, S., et al. 2025, A&A, 693, A188
Sirianni, M., Jee, M. J., Benítez, N., et al. 2005, PASP, 117, 1049
Smith, D. J. B., Dunne, L., da Cunha, E., et al. 2012, MNRAS, 427, 703
Smith, M. G., & Weedman, D. W. 1970, ApJ, 161, 33
Soler, J. D., Zari, E., Elia, D., et al. 2023, A&A, 678, A95
Terlevich, R., & Melnick, J. 1981, MNRAS, 195, 839
Tody, D. 1986, Proc. SPIE, 627, 733
Tody, D. 1993, in Astronomical Data Analysis Software and Systems II, ed. R. J. Hanisch, R. J. V. Brissenden, & J. Barnes, Vol. 52 (San Francisco, CA: ASP), 173
Tomičić, N., Ho, I. T., Kreckel, K., et al. 2019, ApJ, 873, 3
Treyer, M., Schiminovich, D., Johnson, B. D., et al. 2010, ApJ, 719, 1191
van der Hulst, J. M., Kennicutt, R. C., Crane, P. C., & Rots, A. H. 1988, A&A, 195, 38
Vázquez, G. A., & Leitherer, C. 2005, ApJ, 621, 695
Voges, E. S., & Walterbos, R. A. M. 2006, ApJL, 644, L29
Walterbos, R. A. M., & Greenawalt, B. 1996, ApJ, 460, 696
Wang, B., & Heckman, T. M. 1996, ApJ, 457, 645
Weingartner, J. C., & Draine, B. T. 2001, ApJ, 548, 296
Whitmore, B. C., Chandar, R., Kim, H., et al. 2011, ApJ, 729, 78
Whitmore, B. C., Gilmore, D., Leitherer, C., et al. 2005, AJ, 130, 2104
Wofford, A., Charlot, S., Bruzual, G., et al. 2016, MNRAS, 457, 4296
Zavala, J. A., Casey, C. M., Manning, S. M., et al. 2021, ApJ, 909, 165
Zhang, K., Yan, R., Bundy, K., et al. 2017, MNRAS, 466, 3217
Zhu, Y.-N., Wu, H., Cao, C., & Li, H.-N. 2008, ApJ, 686, 155